Marine Geology 456 (2023) 106971

Contents lists available at ScienceDirect

Marine Geology

journal homepage: www.elsevier.com/locate/margo

Research Article

Monitoring of a sediment plume produced by a deep-sea mining test in shallow water, Málaga Bight, Alboran Sea (southwestern Mediterranean Sea)

Sabine Haalboom [a,*], Henko C. de Stigter [a], Christian Mohn [b], Thomas Vandorpe [c,d], Marck Smit [a], Laurens de Jonge [e], Gert-Jan Reichart [a,f]

[a] NIOZ Royal Netherlands Institute for Sea Research, Department of Ocean Systems, Utrecht University, PO Box 59, 1790, AB, Den Burg, Texel, the Netherlands
[b] Department of Ecoscience, Aarhus University, Frederiksborgvej 399, 4000 Roskilde, Denmark
[c] Flanders Marine Institute (VLIZ), Wandelaarkaai 7, 8400 Oostende, Belgium
[d] Ghent University, Department of Geology, Campus Sterre, building S8, Krijgslaan 281, 9000 Gent, Belgium
[e] Royal IHC Mining, Smitweg 6, 2961 AW Kinderdijk, the Netherlands
[f] Utrecht University, Faculty of Geosciences, 3548, CD, Utrecht, the Netherlands

ARTICLE INFO

Editor: Shu Gao

Keywords:
Deep-sea mining
Polymetallic nodules
Sediment plume
Plume monitoring
Sensor array

ABSTRACT

In this study different experimental designs for monitoring of sediment plumes produced by deep-sea mining are presented. Plumes of sediment stirred up from the seabed by mining machines are considered to represent a major environmental pressure which may extend far beyond the actual mining area. Two industry field tests with the scaled mining vehicle *Apollo II* of Royal IHC conducted in a relatively shallow setting offshore southern Spain provided valuable insights for anticipated monitoring of nodule mining activities in the deep Pacific. Although the tests were performed in only 300 m water depth, much less than the depth where future deep-sea mining will take place, the weakly stratified bottom water, tide-dominated near-bed currents with mean magnitude of around 5–10 cm s^{-1}, and gently sloping seabed covered with fine muddy sediment provide a good analogue to operational conditions in the deep sea. The plume of suspended sediment mobilised by the mining vehicle was monitored with turbidity sensors deployed on a ship-operated CTD system and on a static array of moored sensors and monitored visually using a ship-operated ROV. It was found that the generated sediment plume extended no >2 m above the seabed close to the source (<100 m) but increased in height at greater distance. Furthermore, turbidity values decreased rapidly with increasing distance to the source. Even though plume monitoring suffered interference from bottom trawling activities in neighbouring areas, a distinct turbidity signal generated by the mining equipment could still be distinguished above background turbidity at 350 m away from the source. From the experience gained in shallow water, recommendations are made on how a combination of sensors operated from moving and moored platforms may be a suitable and successful strategy for monitoring man-made sediment plumes in the deep sea.

1. Introduction

Concerns about future access to strategic raw materials for the high-tech industry have led to renewed interest in mining of mineral resources from the deep sea as a potential alternative for land-based mining (e.g. Hoagland et al., 2010). Polymetallic nodules, especially abundant in the eastern equatorial Pacific Ocean in water depths of 4000–6000 m, are a likely target of future deep-sea mining (e.g. Glover and Smith, 2003). Polymetallic nodules contain critical raw materials including nickel, copper, cobalt, and manganese in addition to considerable quantities of rare earth elements (e.g. Hein et al., 2013). Polymetallic nodule harvesting from deep-sea environments at an industrial scale is a technological and environmental challenge. Until present, no integrated system for nodule extraction from extreme deep-sea environments including nodule collection, vertical transport and surface processing has reached industrial viability. Furthermore, a legally binding framework regulating extraction of deep-sea mineral resources in areas beyond national jurisdiction, including important aspects such

* Corresponding author.
E-mail address: sabine.haalboom@nioz.nl (S. Haalboom).

https://doi.org/10.1016/j.margeo.2022.106971
Received 1 August 2022; Received in revised form 17 December 2022; Accepted 18 December 2022
Available online 21 December 2022

as management of waste disposal, minimizing environmental impact, and safeguarding ecological preservation, is still in preparation by the International Seabed Authority (ISA) in line with requirements of UNCLOS (ISA - International Seabed Authority, 2019). Many questions exist about possible environmental impacts of deep-sea mining, as it would involve the removal of hard substrate, disturbance of the surface sediment layer, and dispersion of mobilised sediment over large areas of seabed adjacent to the mining site (Levin et al., 2016). To date, impacts and effects of deep-sea mining inside the directly mined area are poorly understood. Estimating mining-related impact in open oceanic regions outside mined areas is even more challenging due to uncertainties of the mining impact scale (Gollner et al., 2017). This mainly concerns the fate and dispersal of sediment-laden near-bottom and mid-water plumes from nodule collection and return of excess sedimentary material after nodule separation. Different ecological risks have been previously highlighted (Jones et al., 2017), including burial of organisms, clogging of suspension feeders and masking of bioluminescence (Washburn et al., 2019). The combined effects of nodule removal and sediment plume deposition may reduce biodiversity and standing stock at the landscape scale (Simon-Lledo et al., 2019). Polymetallic nodule mining at an industrial scale and complementary monitoring of the deep-sea ecosystems and plume propagation have not begun anywhere in the world's oceans. Thus, mining tests and associated monitoring inside a small test area provide a vital baseline for determining the full spatial extent and impact of plumes (Gjerde et al., 2016). Previous impact experiments have contributed to the development of sediment plume models (e.g. Lavelle et al., 1982; Brockett and Richards, 1994; Jankowski et al., 1996; Barnett and Suzuki, 1997), but often have mainly focussed on sediment redeposition (e.g. Yamazaki et al., 1997; Rolinski et al., 2001). Plume modelling in deep-sea environments is ambitious due to a shortage of physical data for model validation and interpretation. Thus, both in-situ baseline data from prospective mining sites yet undisturbed by deep-sea mining and data from monitoring during mining equipment tests and full-scale mining operations are needed to close the existing data gaps and to improve model skills (Gjerde et al., 2016). This again proves the necessity of smaller-scale impact experiments, from which the observations can be used to build and validate models of plume behaviour and dispersion. The reliability of these models will depend on realistic boundary conditions and sediment characteristics obtained from in-situ near-field tests (particle size distribution, sediment release depth and flux, settling velocities, realistic mining scenario) and environmental conditions in the surrounding far-field (bathymetry, ocean currents). Such a combined observation and model approach was successfully applied in a number of recent deep-sea mining related studies in the Clarion-Clipperton Zone (CCZ) (Aleynik et al., 2017; Gillard et al., 2019; Purkiani et al., 2021; Baeye et al., 2022), Tropic Seamount (Spearman et al., 2020) and the Southern California Bight (Kulkarni et al., 2018). Observations on sediment plume dispersion acquired during tests with industrial mining machinery could help to improve existing numerical models, as well as serving as input for future modelling approaches.

Anticipating full-scale industrial mining tests, of which the nodule collector trials by DEME-GSR in the deep Pacific Ocean in spring 2021 heralded the beginning (DEME Group, 2021), we tested approaches for environmental monitoring of mining activities during two industry field tests in relatively shallow waters (about 300 m water depth) offshore southern Spain, carried out in the framework of the European H2020 Blue Nodules project. These field tests, involving technical validation of the scaled polymetallic nodule mining vehicle *Apollo II* developed by the Dutch shipbuilder and maritime technology provider Royal IHC, provided an opportunity to monitor the dispersion of sediment plumes generated by the vehicle. Data on current regime and turbidity collected during the field tests is currently used for numerical modelling of the dispersion of generated sediment plumes. In this paper, we present the experimental setup consisting of static mooring arrays deployed at the seabed and complementary remotely operated vehicle (ROV), and ship-based measurements in the water column with conductivity, temperature, and depth (CTD) profilers, as well as ship-based acoustic Doppler current profiler (ADCP) measurements. Based on our results we point out advantages and shortcomings of the experimental setup and make recommendations for monitoring of sediment plumes in operational settings in the deep sea.

2. Study area

The test area is located on the northwestern Alboran Sea continental slope, about 10 nm south of Málaga, Spain, where the water depth is around 300 m (Fig. 1). The western Alboran Sea is an area of complex water mass and flow dynamics where the deep outflow of high-saline Mediterranean Sea waters through the Strait of Gibraltar is balanced by the near-surface inflow of less saline and colder water masses from the Atlantic (e.g. Vargas-Yanaz et al., 2002; Ercilla et al., 2016; Millot, 2009). The clockwise western Alboran Gyre is the dominant mesoscale circulation feature in the area, extending from east of the Strait of Gibraltar throughout the entire Alboran Basin (Millot, 1999; Renault et al., 2012; Supplement Fig. 1). It is a quasi-permanent feature with little seasonal or inter-annual variability (Supplement Fig. 1). The western Alboran Gyre is most pronounced in the upper 200 m of the water column with maximum current speeds of up to 1 m s^{-1} and is composed of surficial Atlantic Water (AW), modified by mixing with high salinity Mediterranean waters (Millot, 2009). At greater depths, westward propagation of Mediterranean waters in deeper layers compensate the inflow of modified AW. The main deeper water masses are Levantine Intermediate Water (LIW) and Western Mediterranean Deep Water (WMDW). LIW originates in the Levantine Basin in the eastern Mediterranean, flows along the Spanish continental margin in the depth range of 200–600 m and is characterised by salinities exceeding 38.4 in the Western Alboran Sea (Millot, 2009). WMDW has a maximum salinity of 38.4 and is formed in the Western basins of the Mediterranean, spreading along the Moroccan and Spanish continental margin at depths >600 m (Millot, 2009). Tidal currents are generally weak in the Mediterranean Sea (<2 cm s^{-1}) but can be significant in the Alboran Sea with semi-diurnal tidal amplitudes occasionally exceeding 5 cm s^{-1} (Poulin et al., 2018). Other oscillatory motions are associated with internal solitary waves generated over the Camarinal Sill in the Strait of Gibraltar propagating into the western Alboran Sea, which at spring tide may exceed 100 m in vertical amplitude (Sánchez-Garrido et al., 2011). They are well detectable in our field test area but cannot be found eastward of 4°W (van Haren, 2014).

Ercilla et al. (2016) provide a general overview of the geomorphology and sedimentology in the western Alboran Sea and evaluated the role of bottom currents in shaping the Spanish and Moroccan continental margins. Muddy sand and gravel supplied by rivers are the dominant sediment types on the shelf east of Málaga (Bárcenas, 2011), and most likely also on the shelf further to the west. Beyond the shelf break, which is located at 90 m depth in the Málaga Bight, the sediment consists of hemipelagic mud (Baraza et al., 1992; Masqué et al., 2003). The field test area is located on the very gently sloping upper slope (<1°), away from dynamic sedimentary environments such as canyons and channels. The absence of uneven and/or steep terrain in combination with gentle background sedimentation rates render the area suitable for driving with *Apollo II*. From automatic identification systems (AIS) data, the selected area appeared to have relatively low maritime traffic intensity as compared to more near-shore areas (MarineTraffic – Global Ship Tracking Intelligence; www.marinetraffic.com). However, AIS tracks in the vicinity of the test area parallel to the bathymetric contours, indicate (local) fishing activity, in particular bottom trawling. This was confirmed by our own observations of trawlers active at short distance from our test area and is also supported by observations done by Brennan et al. (2015) who visually observed seabed disturbance by bottom trawlers in the area. The trawling results in substantial sediment resuspension and consequently background turbidity values which are much higher than in the deep-sea areas where no bottom trawling takes

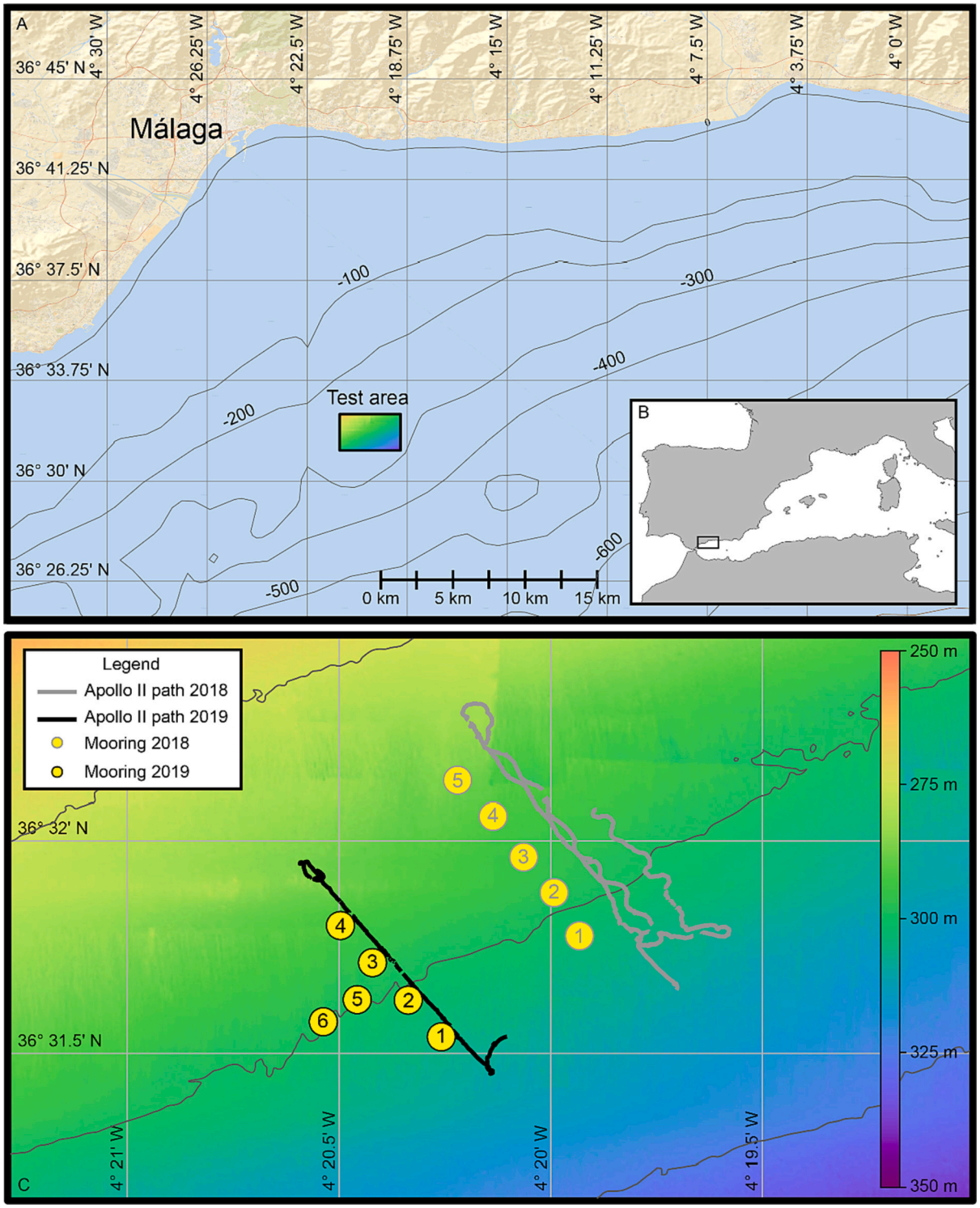

Fig. 1. A) Bathymetric map of the Málaga Bight, SW Mediterranean Sea, with location of the Blue Nodules test site (Google Maps). Location of the test area in the western Mediterranean Sea is shown in B. C) The location of the moorings and the path driven by Apollo II during the drive-by experiments of 2018 and 2019. The isobath contours are given for 275 m, 300 m, and 325 m depth. (For interpretation of the references to colour in this figure legend, the reader is referred to the web version of this article.)

place (Puig et al., 2012; Mengual et al., 2016; Daly et al., 2018).

3. Experimental design

Two industry field tests of Royal IHC's *Apollo II* scaled polymetallic nodule mining vehicle, carried out onboard RV *Sarmiento de Gamboa* in August 2018 and 2019, provided an opportunity to monitor environmental effects arising from usage of this type of deep-sea mining equipment. Monitoring of the sediment plume generated by *Apollo II* comprised vessel-based measurements using CTD and ROV as mobile sensor platforms, and an array of sensors moored at the seabed. The mooring array was equipped with several sensors to record current

speed and direction, as well as turbidity. The ROV provided visual observations of the environmental impacts. Usage of a CTD-Rosette system allowed for profiling of water column properties and collection of water samples. A shipboard ADCP (S-ADCP) provided water column current speed and direction.

3.1. The Apollo II scaled mining vehicle

Royal IHC's *Apollo II* is a scaled pre-prototype mining vehicle with a hydraulic nodule collector (Fig. 2; Boschen et al., 2020). This mining vehicle is 5.6 × 2.5 × 2.3 m in size and weighs 3800 kg in air and 850 kg in water. The mining vehicle is remotely operated through an umbilical cable, enabling hoisting, power supply and data exchange. Propulsion of the vehicle is by four caterpillar tracks, which exert an average pressure of 2.8 kPa on the seabed. During the tests, *Apollo II* was driving at variable speeds up to 0.55 m s^{-1}, with an average speed of 0.25 m s^{-1}. Underwater navigation was done based on propulsion system data and compass readings relayed through the umbilical, whilst a Global Acoustic Positioning System (GAPS) transponder provided underwater position during the tests. The 1 m wide hydraulic nodule collector makes use of powerful jets of seawater to lift the nodules from the seabed. Water flow through the collector is regulated by varying pump rates. The standoff height of the collector relative to the seabed could not be remotely adjusted during the tests but was mechanically adjusted on board the vessel. Since polymetallic nodules are not present in the field test area, only the erosion of the surface sediment layer by the collector could be tested. Sediment taken up by the collector is discharged through the diffuser mounted at the rear of the vehicle. The diffuser is designed to minimise plume development by reducing the discharge flow velocity and aiming the density flow downwards. In order to determine the suspended particulate matter (SPM) mass concentration in the immediate vicinity of *Apollo II*, a JFE Advantech Infinity optical backscatter sensor (OBS) was mounted to the diffuser to record the turbidity at a sampling rate of 1 min. Furthermore, in 2018, a Nortek Aquadopp 2 MHz current profiler was mounted on the diffuser. During the drive-by in front of the moorings on the 18th of August, the sensor was mounted with its head facing backwards, whereby two of the beams were directed downwards towards the seabed and one beam was directed upwards. This allowed for recording echo amplitude profiles behind the diffuser of the *Apollo II*, at a sampling rate of 5 min.

3.2. ROV Zonnebloem

The ROV *Zonnebloem* (formerly called ROV *Genesis*) of the Flanders Marine Institute (VLIZ) was used for performing video surveys of the seabed at the field test site before and after passage of *Apollo II*, for technical inspections during deployments of *Apollo II*, and for observations of the sediment plume generated by *Apollo II*, while it was driving over the seabed. It is a 2000 m depth-rated CHEROKEE ROV with a Tether Management System (TMS) built by the company Sub-Atlantic. For video observations, the ROV was equipped with a Luxus HD Zoom forward-looking video camera, mounted on a pan-and-tilt unit and two SD Luxus compact cameras installed at the rear and on front of the ROV.

3.3. Underwater positioning

Sub-meter navigation of the *Apollo II* and the ROV and positioning of the box corer used for sediment coring was performed using an IXBLUE GAPS and transponders mounted on each of the platforms. The calibration-free GAPS is a portable Ultra Short Base Line (USBL) with integrated Inertial Navigation System. The GAPS was mounted and deployed from the drop-keel of RV *Sarmiento de Gamboa* and received the ship's onboard GPS signal. Underwater positioning was obtained every second and all positioning data (ship and GAPS) was immediately visualized.

3.4. Water column profiling and sampling

3.4.1. CTD-Rosette

The SeaBird 911+ CTD-Rosette system of RV *Sarmiento de Gamboa* was lowered through the water column for profiling of water properties, including while the *Apollo II* was driving, targeting the plume generated by the mining vehicle (Fig. 3). Water samples for collection of SPM were taken at discrete water depths using the 12 L Niskin bottles integrated in the CTD-Rosette system. The CTD-frame was equipped with two turbidity sensors, a WetLabs ECO FLNTU OBS integrated with the standard sensor package and a JFE Advantech Infinity OBS mounted at the base of the CTD frame. A second JFE Advantech OBS was suspended

Fig. 2. Deployment of the *Apollo II* pre-prototype nodule collector vehicle from the aft of RV *Sarmiento de Gamboa* during the 2018 field test in Málaga Bight. Photo courtesy: Alberto Serrano. Note the Nortek Aquadopp current profiler mounted upward-facing on starboard side of the diffuser. Acoustic backscatter data presented in Fig. 11E were acquired with the current profiler mounted backward-facing.

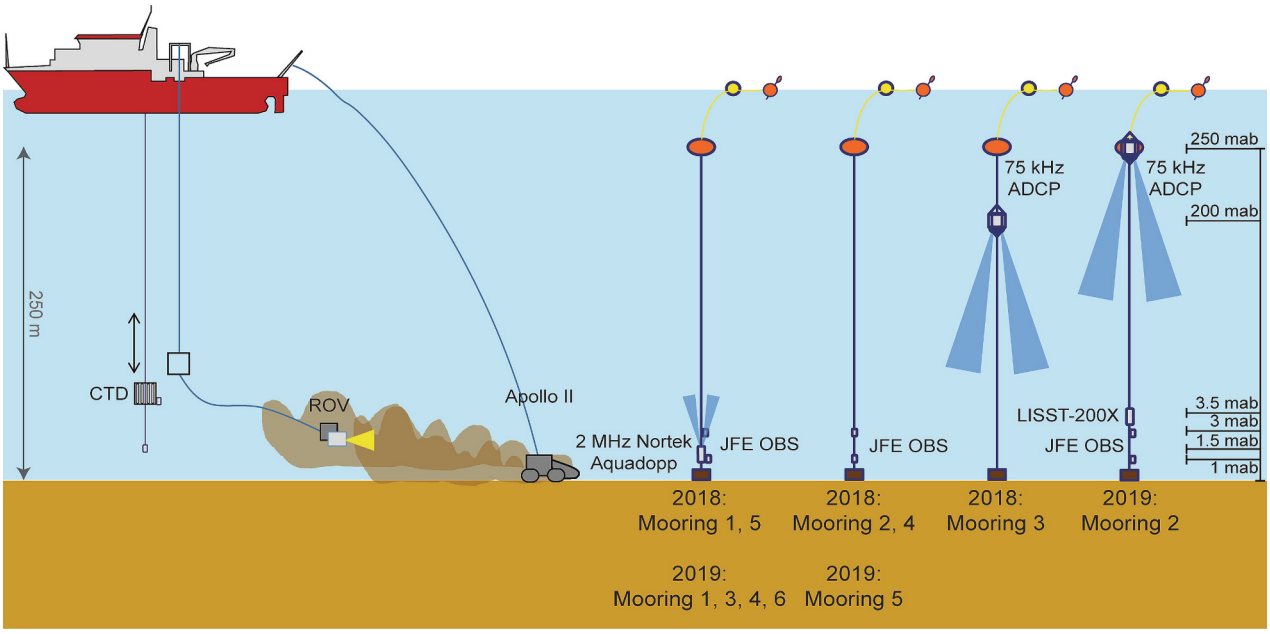

Fig. 3. Schematic overview of the plume monitoring setup. *Apollo II* was driven along the mooring array equipped with turbidity sensors, current profilers, sediment traps, LISST and acoustic recorder, while RV *Sarmiento de Gamboa* was following, moving backwards. During this operation, the CTD or ROV equipped with additional turbidity sensors were alternatingly deployed for monitoring the plume.

below the CTD-frame to record turbidity as close to the seabed as possible (one metre above bed, mab). In 2018, a Sequoia LISST-200X in-situ particle sizer was mounted at the base of the CTD frame during three CTD casts for in-situ observations of SPM particle size distribution. Additionally, the LISST-200X recorded turbidity using a transmissometer. In total 33 full water column CTD casts were collected, 18 in 2019 and 15 in 2019 (Supplement Table 1). Nineteen of the 33 CTD casts were carried out from a moving ship following the mining vehicle, aiming to capture the sediment plume generated by the *Apollo II*. Various approaches, tow-yo-ing the CTD between surface and 4 mab, towing the CTD at 4 mab, tow-yo-ing between 4 and 10 mab, tow-yo-ing between 2 and 15 mab, were done to acquire profiles and water samples from the sediment plume created by *Apollo II*.

Water samples taken during the CTD casts were used for determining the SPM mass concentration inside- and outside of the generated sediment plume, as well as the background turbidity. From each collected 12 L Niskin bottle, two subsamples of maximum 5 L were drawn. These subsamples were vacuum filtered on board over pre-weighed 47 mm polycarbonate filters with a pore size of 0.4 µm, applying 0.3 Bar underpressure. After filtration the filters were rinsed with Milli-Q water, and subsequently left to dry in a Flowtronic laminar flow bench. In the laboratory, the filters were rinsed once more with Milli-Q water to remove any remaining salt and then freeze-dried. Afterwards the filters were weighed in duplo, or in triplo if the difference between the first two measurements was >0.03 mg. To yield SPM mass concentrations, the net dry weight of the SPM collected on the filters, corrected by the average weight change of all blank filters, was divided by the volume of filtered seawater.

3.4.2. Shipboard ADCP

Shipboard ADCP data were collected continuously in 2018 and 2019 throughout the entire survey period (8–19 August 2018, 12–25 August 2019). On-station and underway current velocity components were collected in the water column with a 75 kHz Teledyne RD Instruments (RDI) Ocean Surveyor system mounted in the hull of RV *Sarmiento de Gamboa* along with ancillary data of ship position and motion (pitch, roll and heading). The software RDI VmDAS was used to configure instrument setup, data communication (ship position, ship heading) and data acquisition. The vertical bin size was set to 8 m (first bin at 25 m, transducer depth 9 m) and the total sampling range was 100 bins (800 m). The transducer offset relative to the ship's keel was 46.33°. Repeated underway ADCP surveys were conducted mostly during night-time along a rectangle (6.25 km *E*-W x 7.78 km N-S) set around the actual test site. On-station time series were collected at the field test site inside the underway rectangle mainly during daytime.

S-ADCP data were processed and analysed daily on board to provide near real-time estimates of structure and variability of currents in support of the in-situ monitoring. Processing of single ping S-ADCP data was conducted using the Common Oceanographic Data Access System (CODAS) from the University of Hawaii (Firing et al., 1995; http://currents.soest.hawaii.edu/docs/adcp_doc/index.html) following the GO-SHIP guidelines for S-ADCP measurements (Firing and Hummon, 2010). The main CODAS processing steps included time-averaging of single ping data into 120 s ensembles, water track calibration to estimate any remaining transducer offset and calculating absolute current velocities by removing the ship velocity from the ADCP ensemble velocities. Finally, depth bins with a percent good value <20% of the acoustic return signal were discarded to eliminate effects from strong interference of the acoustic signal with the seabed (Mohn et al., 2018). As a consequence, velocity data from the lower 3 bins (24 m) above bottom were discarded.

3.4.3. Sediment sampling

For analysis of particle size distributions in the surface sediment, sediment cores were collected by means of a NIOZ 'HaJa' box corer. The cylindrical coring barrel of 30 cm diameter and height of 55 cm is closed off on both ends upon retrieval from the seabed, preserving the sediment core with overlying water relatively undisturbed. In total 12 successful box corer casts were made and from each of the cores in 2018, and from 5 of the 7 cores taken in 2019, a 6 cm diameter subcore was taken. Sediment particle size distribution was determined for the top 1 cm of each subcore with the Beckman Coulter LS13 320 at NIOZ. About 250 mg of wet sediment was immersed in a beaker with 20 mL of reverse osmosis (RO) water and dispersed without application of ultrasonic or chemical dispersant. The suspension was introduced in the large volume cell of the particle sizer, and particle size distributions were calculated

Table 1
Overview of the used sensors, with specifications on measurement settings and deployment.

Name	Year	Platform	Equipment	Depth	Measuring range	Settings
BN18-L3	2018	Apollo II (L3)	JFE Advantech OBS	1.65 mab	Spot measurement	5 min interval, 30 samples, 1 Hz
			Nortek Aquadopp	2.40 mab	2.9–12.9 mab	5 min interval, 60 samples, 1 Hz, 20 bins, 0.5 m bin size, 0.5 m blanking distance
BN18-L5	2018	Apollo II (L5)	JFE Advantech OBS	1.75 mab	Spot measurement	1 min interval, 15 samples, 1 Hz
			Nortek Aquadopp	1.75 mab	0.5–10.5 m	1 min interval, 30 samples, 1 Hz, 48 bins, 0.2 m bin size, 0.1 m blanking distance
BN18-M1	2018	M1	JFE Advantech OBS	1 mab	Spot measurement	1 min interval, 15 samples, 1 Hz
			JFE Advantech OBS	3 mab	Spot measurement	1 min interval, 15 samples, 1 Hz
			Nortek Aquadopp	1.5 mab	2 mab – 12 mab	1 min interval, 30 samples, 1 Hz, 20 bins, 0.5 m bin size, 0.5 m blanking distance
BN18-M2	2018	M2	JFE Advantech OBS	1 mab	Spot measurement	1 min interval, 15 samples, 1 Hz
			JFE Advantech OBS	3 mab	Spot measurement	1 min interval, 15 samples, 1 Hz
BN18-M3	2018	M3	RDI Workhorse ADCP	200 mab	0 mab – 175 mab	5 min interval, 11 pings, 0.04 Hz, 15 bins, 16 m bin size, 24.8 m blanking distance
BN18-M4	2018	M4	JFE Advantech OBS	1 mab	Spot measurement	10 min interval, 15 samples, 1 Hz
			JFE Advantech OBS	3 mab	Spot measurement	10 min interval, 15 samples, 1 Hz
BN18-M5	2018	M5	JFE Advantech OBS	1 mab	Spot measurement	10 min interval, 15 samples, 1 Hz
			JFE Advantech OBS	3 mab	Spot measurement	10 min interval, 15 samples, 1 Hz
			Nortek Aquadopp	1.5 mab	2 mab – 12 mab	1 min interval, 30 samples, 1 Hz, 20 bins, 0.5 m bin size, 0.5 m blanking distance
BN19-M1	2019	M1	JFE Advantech OBS	1 mab	Spot measurement	1 min interval, 15 samples, 1 Hz
			JFE Advantech OBS	3 mab	Spot measurement	1 min interval, 15 samples, 1 Hz
			Nortek Aquadopp	2 mab	2.5 mab – 12.5 mab	1 min interval, 60 samples, 1 Hz, 20 bins, 0.5 m bin size, 0.5 m blanking distance
BN19-M2	2019	M2	JFE Advantech OBS	1 mab	Spot measurement	1 min interval, 15 samples, 1 Hz
			JFE Advantech OBS	3 mab	Spot measurement	1 min interval, 15 samples, 1 Hz
			LISST-200X	3.5 mab	Spot measurement	1 min interval, 60 samples, 1 Hz
			RDI Workhorse ADCP	250 mab	0 mab – 237 mab	2 min interval, 60 pings, 2 Hz, 74 bins, 4 m bin size, 12.71 m blanking distance
			Devologic Sono Vault acoustic recorder	10 mab	Spot measurement	Continuous sampling
BN19-M3	2019	M3	JFE Advantech OBS	1 mab	Spot measurement	1 min interval, 15 samples, 1 Hz
			JFE Advantech OBS	3 mab	Spot measurement	1 min interval, 15 samples, 1 Hz
			Nortek Aquadopp	2.5 mab	3 mab – 13 mab	1 min interval, 60 samples, 1 Hz, 20 bins, 0.5 m bin size, 0.5 m blanking distance
BN19-M4	2019	M4	JFE Advantech OBS	1 mab	Spot measurement	1 min interval, 15 samples, 1 Hz
			JFE Advantech OBS	3 mab	Spot measurement	1 min interval, 15 samples, 1 Hz
			Nortek Aquadopp	2.5 mab	3 mab – 13 mab	1 min interval, 60 samples, 1 Hz, 20 bins, 0.5 m bin size, 0.5 m blanking distance
			PPS4/3 Sediment trap	2.5 mab		Start: 20-08-2019 07:45, sampling interval: 1 h
BN19-M5	2019	M5	JFE Advantech OBS	1 mab	Spot measurement	1 min interval, 15 samples, 1 Hz
			JFE Advantech OBS	3 mab	Spot measurement	1 min interval, 15 samples, 1 Hz
			PPS4/3 Sediment trap	2.5 mab		Start: 20-08-2019 08:00, sampling interval: 1 h
BN19-M6	2019	M6	JFE Advantech OBS	1 mab	Spot measurement	1 min interval, 15 samples, 1 Hz
			JFE Advantech OBS	3 mab	Spot measurement	1 min interval, 15 samples, 1 Hz
			Nortek Aquadopp	2 mab	2.5 mab – 12.5 mab	1 min interval, 60 samples, 1 Hz, 20 bins, 0.5 m bin size, 0.5 m blanking distance

applying an optical model (called: grey), which uses an average of refractive indices of the most common minerals including quartz, calcite, feldspar and mica, suited for fine-grained sediment. Particle size distribution is reported as volume percentage of particles within logarithmic size classes from 0.4 to 2000 μm, assuming spherical particles.

3.5. Mooring array

Different mooring setups were tested for monitoring of the temporal evolution and spatial extent of sediment plumes created by the *Apollo II* test vehicle. The moorings consisted of a 760 kg steel anchor weight, directly attached (2018) or attached via a single IXSea acoustic release (2019) to a 250 m long mooring line, the latter held up in the water column by a 150–250 kg "smartie" float of syntactic foam, to which an additional 50–70 m long floatline with surface floats was attached. Accurate positioning on the desired location, which in 2019 could be confirmed by acoustic ranging of the releases, was done by lowering the mooring string with anchor weight first to the seabed. In 2018, five moorings were distributed with a 200 m interval along a single 800 m SE-NW trending line parallel to the intended driving path of the vehicle and perpendicular to the expected prevailing current directions (Fig. 1; Supplement Fig. 2). By driving *Apollo II* at different distances along the mooring array, the characteristics of the proximal and more distal plume would be recorded. In 2019, six moorings were deployed in a T-shaped array (Fig. 1; Supplement Fig. 2). Four of these on a 600 m long, SE-NW trending line oriented at right angles to the isobaths and parallel to the intended driving path of the vehicle and perpendicular to the expected prevailing current direction, with the moorings 200 m apart from each other. Two were placed perpendicular to this first line at 150 and 300 m distance, respectively. In this configuration, a single drive-by would suffice to record both the proximal and the more distal plume.

The application of different types of sensors on the moorings and on mobile platforms is illustrated in Fig. 3. Sensor settings are given in Table 1. To record turbidity and current speed and direction, 4 moorings in 2018 and 6 in 2019 were equipped with JFE Advantech OBSs at 1 and 3 mab, 4 moorings with upward-looking 2 MHz Nortek Aquadopp current profilers at 2 mab and one mooring with a downward-looking 75 kHz RDI Workhorse Long Ranger ADCP mounted at 250 mab (2018) and 250 mab (2019). In addition to that, 2 moorings were equipped with Technicaps PPS4/3 sediment traps during both years (BN18-M2, BN18-M4, BN19-M4 and BN19-M5) for collecting settling particulate material. The sediment traps with cylindroconical shape had their 0.05 m^2 opening at 2.5 mab and were each equipped with a carrousel with 12 sampling bottles of 250 mL. The data of the 2018 moorings is not shown here as the sediment traps sampled material when the *Apollo II* was not being operated. In 2019 the sediment traps were set to sample on the 20th of August. Furthermore, in 2019 mooring 2 (BN19-M2) was equipped with a LISST-200X at 3.5 mab for in-situ recording of particle sizes and turbidity and a Develogic Sono Vault deep-sea acoustic recorder at 10 mab for recording underwater noise. The sampling frequency was set to 1 min for the OBSs, Nortek Aquadopp current profilers and LISST. The 75 kHz ADCP had a sampling frequency of 2 min. The Nortek Aquadopp had a sampling range of 10 m, with vertical intervals binned over 0.5 m (20 bins) and a blanking distance of 0.5 m. In 2018, the 75 kHz ADCP had a sampling range of 240 m with vertical intervals binned over 16 m (15 bins) and a blanking distance of 24.8 m. In 2019, the 75 kHz ADCP had a sampling range of 296 m with vertical intervals binned over 4 m (74 bins) and a blanking distance of 12.81 m. Data points collected by the Nortek Aquadopp represent the ensemble average of 60 individual measurements within the sampling interval, for the JFE Advantech OBS this is 15 measurements per ensemble and for the 75 kHz ADCP, respectively for 2018 and 2019, 11 pings per ensemble and 60 pings per ensemble.

3.6. Conversion of optical and acoustic backscatter signal

The linear relationship found between the turbidity signal of WetLabs and JFE Advantech OBSs mounted on the CTD-Rosette system and SPM mass concentration determined by filtration of simultaneously taken Niskin water samples was used to convert the turbidity signal of each individual sensor into SPM mass concentration, following equation (Eq. (1)):

$$SPM\ \left[mg\ L^{-1}\right] = a^{*}Turbidity + b \tag{1}$$

in which *SPM* is the SPM mass concentration in mg L^{-1}, *turbidity* is the output of the OBS sensors in NTU or FTU, and *a* and *b* are constants determined by resolving the relationship between the recorded signal and the determined SPM mass concentration. This was done for each individual sensor, as all of them were lowered on the CTD at least once while during that cast at least 5 Niskin water samples were taken, covering a range of turbidity values. Turbidity values recorded by the LISST-200X (expressed as beam attenuation) have not been converted into SPM mass concentrations.

The echo amplitude (amp) recorded by the Nortek Aquadopp current profilers is explored here for information it provides on the near-bottom gradients in SPM mass concentration. The amp signal was converted to echo level to account for the attenuation by acoustic spreading and water absorption. This was done by following the equation (Eq. (2)) given in the technical note by Lohrmann (2001):

$$Echo\ level\ [dB] = 0.43^{*}amp + 20log_{10}(R) + 2\alpha_{w}R + 20R\int \alpha_{p}dr \tag{2}$$

in which R is the distance along the acoustic beam, α_w the water absorption coefficient and α_p the coefficient of particle attenuation. The water absorption coefficient, α_w, was determined following the model of Ainslie and McColm (1998), with parameters set to an instrument frequency of 2000 kHz, temperature of 13.5 °C, salinity of 38.5 and depth of 300 m, giving an α_w of 1.234 dB m^{-1}.

The particle attenuation coefficient, α_p, dependent on site-specific particle characteristics, was treated as an unknown. In most cases this term can be ignored, especially at lower concentrations as the correction for the loss of attenuation over depth has a far larger effect than the difference in particle attenuation over the ranged profile (Lohrmann, 2001). Therefore, the acoustic backscatter data shown in this study is only corrected for the loss of attenuation due to acoustic spreading and absorption by water (Eq. 3):

$$Echo\ level\ [dB] = 0.43^{*}amp + 20log_{10}(R) + 2\alpha_{w}R \tag{3}$$

4. Results

4.1. Hydrography and current dynamics

The core water masses present in the test area can be clearly distinguished in CTD water column profiles and in a T-S plot comprising all temperature and salinity data recorded with the CTD (Fig. 4): modified AW in the upper 200 m with temperatures of 17–24 °C and salinities of 36.3–36.6, and at depths exceeding 200 m LIW with temperatures of below 13.4 °C and salinities higher than 38.4. S-ADCP water column current measurements in 2018 and 2019 (Supplement Fig. 3 and Fig. 5, respectively) show that *E*-W (u) and N-S (v) velocity components are dominated by semidiurnal internal tides; the resulting currents regularly change from southwest, i.e. along-slope, to northerly, cross-slope, direction (Fig. 5A, B). The surface layers (depths <100 m) were largely out of phase with the deeper layers indicating maximum current shear at around 100 m depth (Fig. 5A-C). A pronounced amplification of current magnitudes in the upper 100 m was recorded in 2019 after 23 August resulting in intensified SW along-slope flow and weaker cross-slope flow. The predominant semi-diurnal variation of currents was

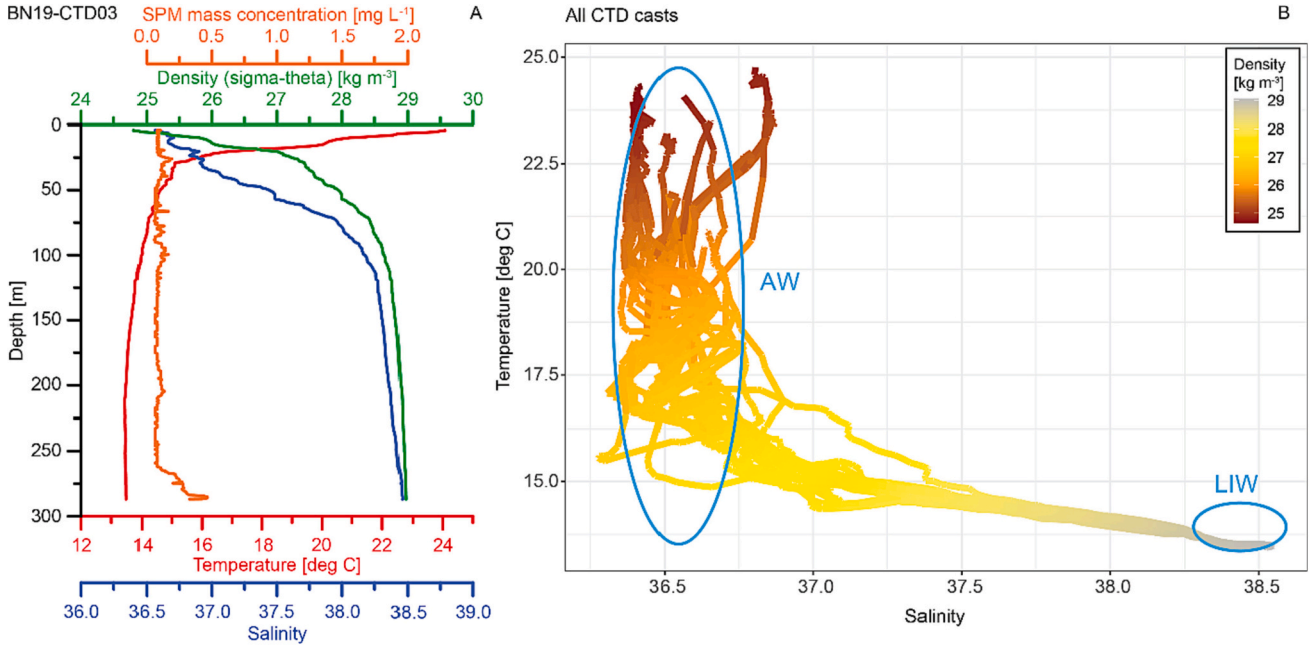

Fig. 4. Water mass characteristics of the Málaga Bight test site. A) Water column profiles of temperature, salinity, density, and SPM mass concentration as observed in CTD cast BN19-CTD03; B) T-S diagram comprising all 2018 and 2019 CTD measurements collected to a maximum depth of 300 m. The observed core water masses are modified Atlantic Water (AW) and Levantine Intermediate Water (LIW). Below 50 m depth AW properties are strongly modified (lower temperatures, higher salinities) due to mixing with LIW. Our sampling did not reach water depths where Western Mediterranean Deep Water (WMDW) could be detected.

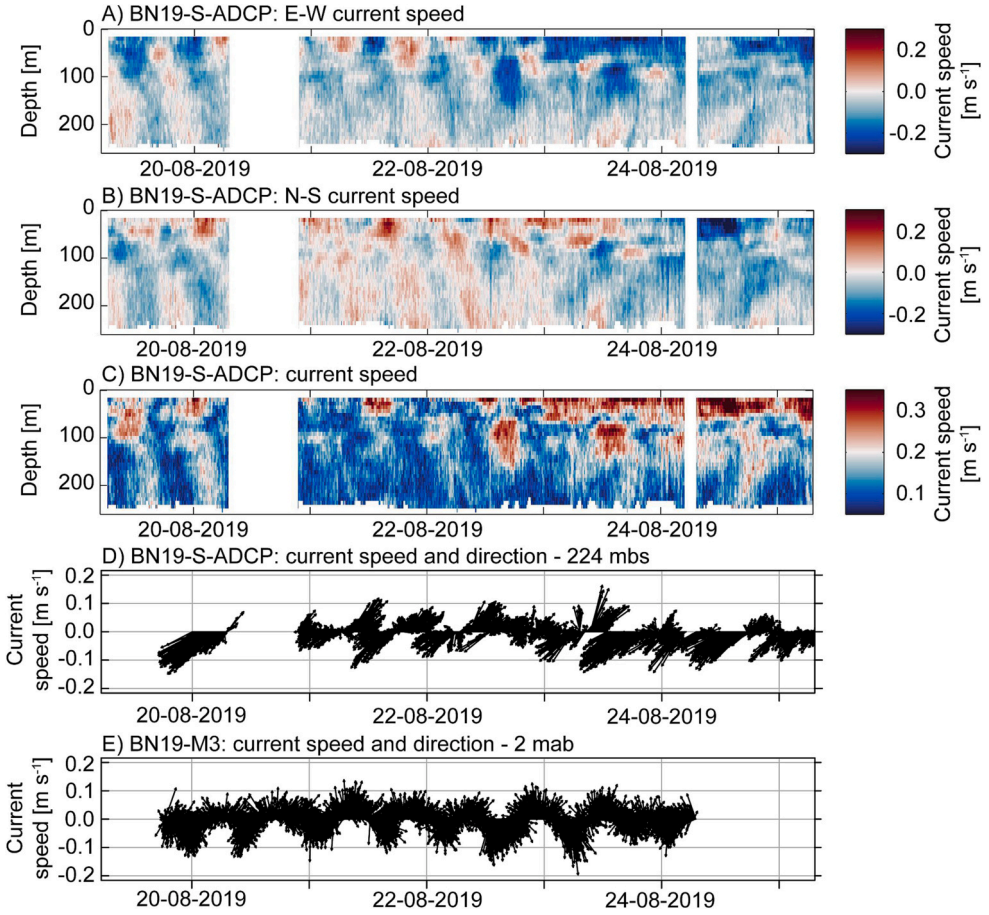

Fig. 5. Current dynamics of the Málaga Bight test site for the period 20–25 August 2019, when the mooring array was deployed. A-C) Time series of, respectively, *E*-W current speed, N-S current speed, and total current speed (m s^{-1}) between 25 and 250 m below sea surface (mbs) recorded by the S-ADCP; D and E) Time series of, respectively, current speed recorded at 224 mbs by the S-ADCP and current speed recorded at 2 mab by the Aquadopp current profiler of mooring BN19-M3.

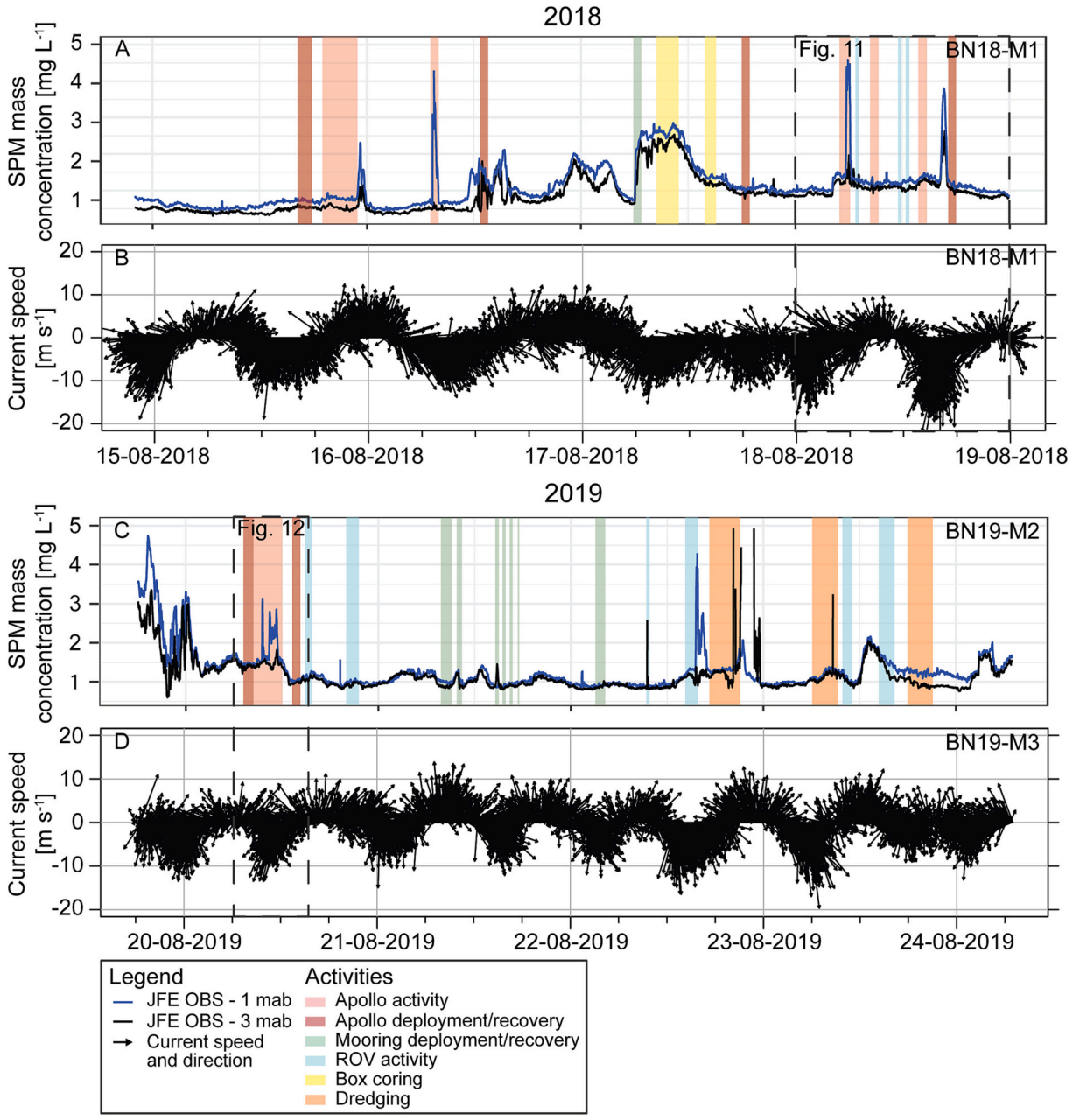

Fig. 6. Time series of SPM mass concentration and current speed and direction in the near-bottom layer as recorded by the JFE OBSs and Aquadopp current profilers in moorings BN18-M1, BN19-M2 and BN19-M3, deployed, respectively, 15–19 August 2018 and 19–24 August 2019. The different coloured bars represent different activities that might have caused resuspension of surface sediments. Data recorded during Apollo II drive-bys are illustrated in more detail in Figs. 11 and 12.

also observed near the bottom in current records obtained with moored Nortek Aquadopp current profilers (Fig. 5E). At all depth levels, the semi-diurnal tidal variation is superimposed on a SW along-slope mean flow.

4.2. Water column turbidity

Apart from shallow turbidity variations in the upper 50 m of the water column associated with pelagic productivity, most of the water column was relatively transparent, with SPM mass concentrations <0.1 mg L^{-1} (Fig. 4). In the lower 10–20 m of the water column, approaching the seabed, a decrease in transparency was observed. Background SPM mass concentration, measured with moored OBSs at 1 mab and excluding intervals when *Apollo II* was active at the bottom, showed conspicuous variation over the few days that the moorings were deployed, generally varying between 0.5 and 2.5 mg L^{-1} in 2018, with occasional peaks up to 5 mg L^{-1} and between 1 and almost 5 mg L^{-1} in 2019 (Fig. 6). With the relatively high background turbidity, it was at times difficult to distinguish the turbidity signal of the plume produced by *Apollo II*. During intervals of high turbidity, visibility was often so reduced that navigation of the ROV *Zonnebloem* close to seabed could not be done on sight but only with help of sonar and altimeter. SPM particle size distribution with the LISST-200X, which in 2018 was mounted in the CTD frame and in 2019 mounted at 3.5 mab in BN19-M2, showed highly variable bimodal distribution patterns (Fig. 7A). In background water without additional SPM stirred up by Apollo II, a relatively fine mode centred around 5 to 10 μm was almost always present, while a more pronounced coarser mode was found to shift back and forth between 50 and 250 μm. The coarsest modes occurred mostly during intervals of high background turbidity.

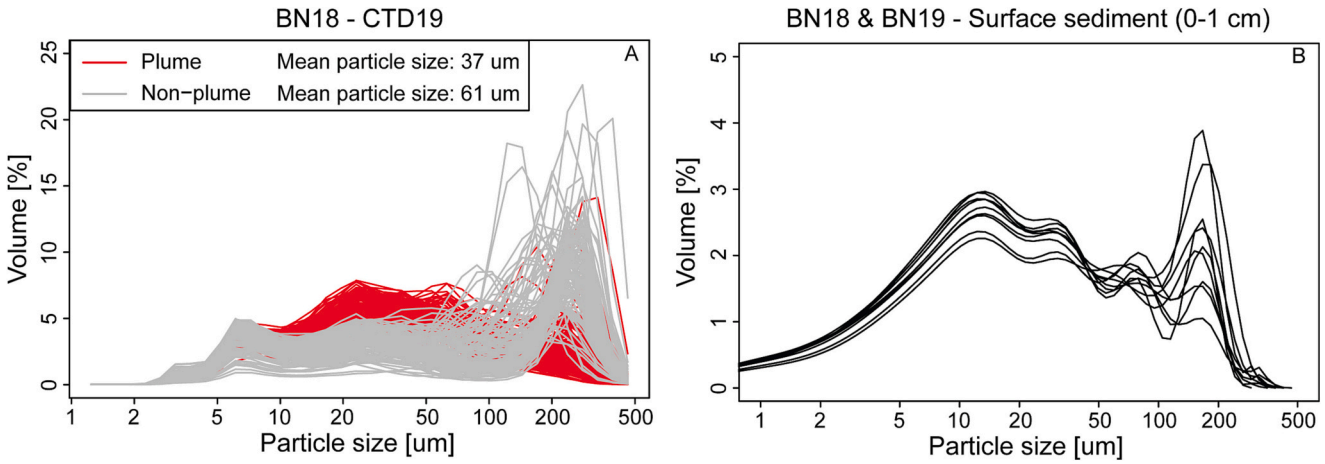

Fig. 7. A) Particle size distribution curves of, respectively, non-plume background SPM (grey) and plume SPM (red) in near-bottom water recorded by LISST-200X on BN19-CTD19 on the 18th of August 2018. The distinction of plume/non-plume SPM is made on the basis of simultaneously recorded turbidity (beam attenuation) by the LISST-200X (see Supplement Fig. 4A). B) Particle size distribution of surface sediment (0–1 cm) of the box cores from 2018 and 2019. (For interpretation of the references to colour in this figure legend, the reader is referred to the web version of this article.)

4.3. Seabed characteristics

From seabed video imagery obtained with ROV and *Apollo II* and box coring results, the weakly sloping seabed of the test area (average slope of 0.9°) appeared uniformly covered with soft clayey silt. The surface sediment recovered in box cores had a bimodal particle size distribution, with a fine-grained mode centred around 12–32 μm and a coarser mode centred around 128–185 μm. Median particle size is 16–30 μm (Fig. 7B). The sand fraction is largely composed of planktonic and benthic foraminifera and rounded glauconite grains, the latter mostly formed as internal casts of foraminifera shells. The sediment surface, as observed with ROV *Zonnebloem* and the forward-looking camera of *Apollo II*, was marked by a conspicuous pit and mound morphology resulting from intense bioturbation by burrowing crustaceans (Fig. 8). Large *Cerianthus* sea anemones were also relatively common (Fig. 8B). Upon approach of *Apollo II* these anemones were seen to retract into the sediment within a split second, an escape behaviour which enables these animals to survive in an intensely trawled area. Other sessile benthic fauna appeared scarce, likely under pressure from the intensive trawling. Trawl marks, including elongate striae produced by the trawl net dragging over the seabed and deep groves ploughed in the seabed by the trawl doors (Fig. 8C), were commonly encountered.

4.4. SPM characteristics and sensor calibration

The turbidity signal recorded with the WetLabs and JFE Advantech OBSs mounted on the CTD-Rosette system generally showed a good linear relationship with SPM mass concentration measured in Niskin water samples taken simultaneously (Fig. 9). R^2 values for the linear fit ranged from 0.74 to 0.92 in 2018 and from 0.88 and 0.97 in 2019 (Fig. 9 and public data in PANGAEA), excluding data from CTD02 of 2019 (red line). Most of the Niskin samples used for sensor calibration probably represent background water. Collecting water samples from the plume turned out to be difficult, because the plume in its initial phase, while it was in reach of the CTD lowered from the ship, did not extend much higher than 2–3 m above the seabed. In order to sample the plume, the CTD-Rosette should have been immersed into the plume, with high risk of hitting the seabed. Only CTD02 in 2019 (red data points in Fig. 9A and B) appeared to have successfully sampled water from within the plume, which is reflected by a conspicuously different relationship of SPM mass concentration vs. turbidity measured with the OBSs. For similar SPM mass concentration, the plume SPM would produce a 2- to 3-fold higher optical backscatter than the SPM of background water.

A quantitative relationship between acoustic backscatter recorded with the moored Nortek Aquadopp current profilers and SPM mass concentration was established indirectly, using SPM mass concentration inferred from JFE Advantech OBS recordings collected simultaneously within the same depth interval as where the acoustic backscatter was collected (Fig. 9). For suspensions with uniform particle composition and size distribution, the relationship between recorded echo level and SPM mass concentration should conform to a logarithmic function of the form:

$$Echo\ level\ [dB] \propto log_{10}(SPM) \quad (4)$$

However, in the SPM and acoustic backscatter data collected in 2018 and 2019, a broad scatter is observed which cannot be described by a single logarithmic relation as in Eq. (4). Rather, in 2018 two main clusters of data can be distinguished, and five clusters in 2019, each conforming to a logarithmic relationship of the general form given in Eq. (4) but with different constants (Fig. 9). The data clusters, representing SPM with different optical and acoustic backscatter characteristics (Fig. 9C and D), correspond to different time intervals in the recorded data (Fig. 9E and F). In 2018 (Fig. 9B), the majority of the data belong to one cluster characterised by a relatively high acoustic backscatter response. A much smaller part of the data belongs to the second cluster, characterised by relatively low acoustic backscatter response. This second cluster represents two short time intervals (Fig. 9E), the first late on August 15th when *Apollo* II landed on the seabed and drove to the start position for a drive-by along the mooring array, the second in the course of August 16th when *Apollo II* performed the actual drive-by which was, however, aborted before completing it. A second, successful, drive-by on 18 August 2018, and the drive-by performed in 2019, do not seem to be reflected in a distinct data cluster (Fig. 9C and D). The cluster with lowest acoustic backscatter in the 2019 data (blue cluster; Fig. 9D) cannot be linked to *Apollo II* activity (Fig. 9F) and must be considered as part of the background variability.

4.5. Plume characteristics near the mining vehicle

SPM mass concentrations measured directly at the rear of the *Apollo II* with a JFE Advantech OBS attached to the diffuser, went up to 100 mg L^{-1} when the vehicle was driving with the hydraulic nodule collector switched on (Fig. 10A). Tow-yo-ing the CTD while following the *Apollo II* mining vehicle at about 100 m distance, gave insight in SPM mass concentration and maximum height of the created sediment plume in its initial phase (Fig. 10B, C and D). The turbidity sensor mounted within

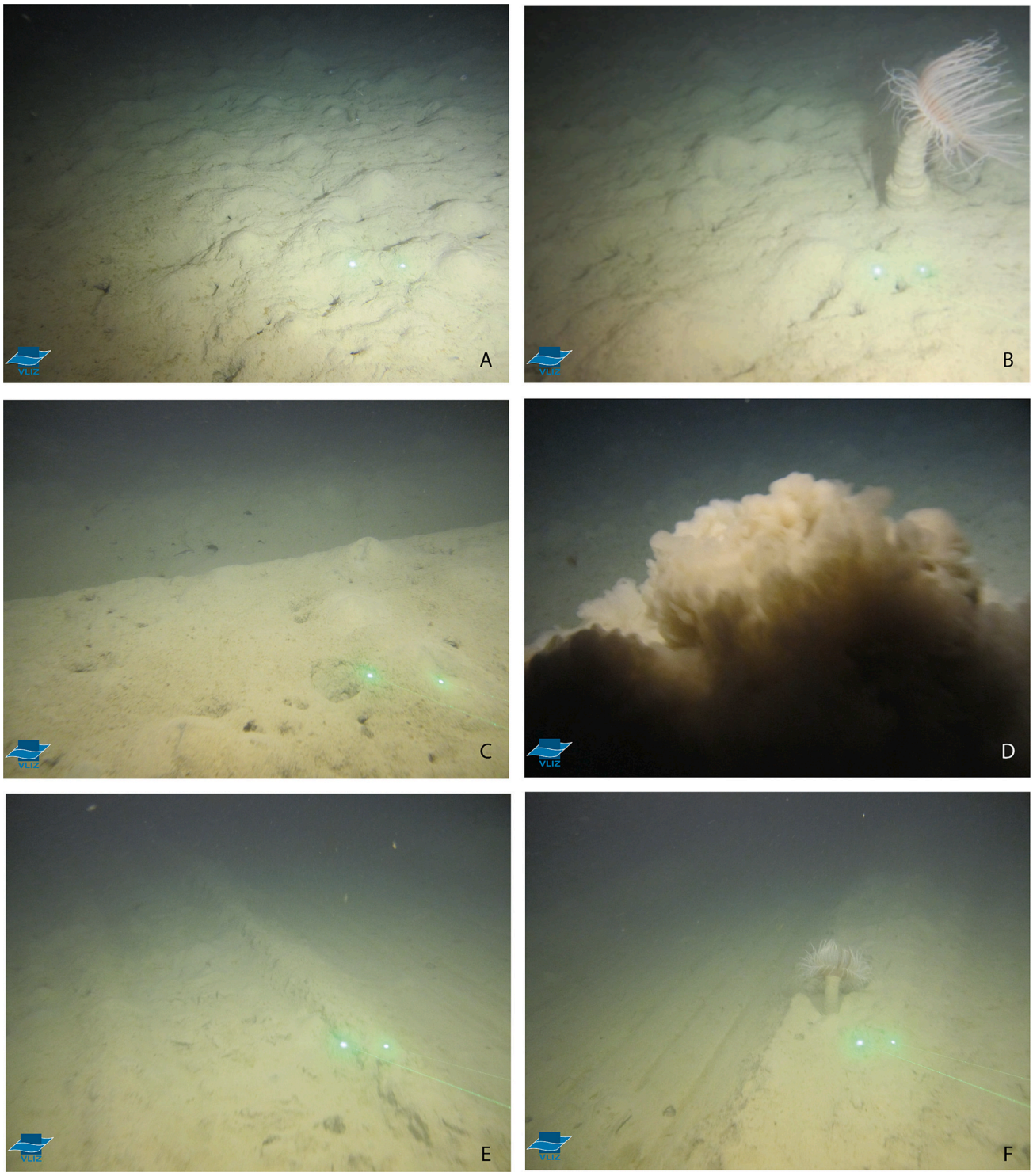

Fig. 8. Seabed images taken by the ROV *Zonnebloem* of VLIZ. A) Undisturbed seabed; B) Undisturbed seabed with a sea anemone; C) Trawl door mark; D) Sediment plume produced by *Apollo II*; E) Imprint by *Apollo II* caterpillar track; F) Imprint by *Apollo II* collector. The green laser dots given for scale are 8 cm apart. (For interpretation of the references to colour in this figure legend, the reader is referred to the web version of this article.)

the CTD frame, which during this cast, illustrated in Fig. 10, only approached the seabed to 4 mab (Fig. 10B), did not show any increase in SPM mass concentration above the natural background SPM mass concentration of about 0.75 mg L^{-1}. However, the turbidity sensor suspended 3 m below the CTD frame, which approached the seabed to about 1 mab, recorded enhanced SPM mass concentration near the bottom (Fig. 10C, D). While the *Apollo II* was driving with its hydraulic nodule collector switched off, a sediment plume was generated only by interaction of the caterpillar tracks with the seabed and by water displacement and turbulence around the vehicle. The SPM mass concentration within the plume, measured at about 100 m behind the vehicle, was generally around 5 mg L^{-1}. With the hydraulic collector switched on, the additional discharge of sediment-laden seawater through the mining vehicle's diffuser resulted in a marked increase in SPM mass concentration within the plume to around 20 mg L^{-1}. The relatively low height of the plume in its initial phase was visually

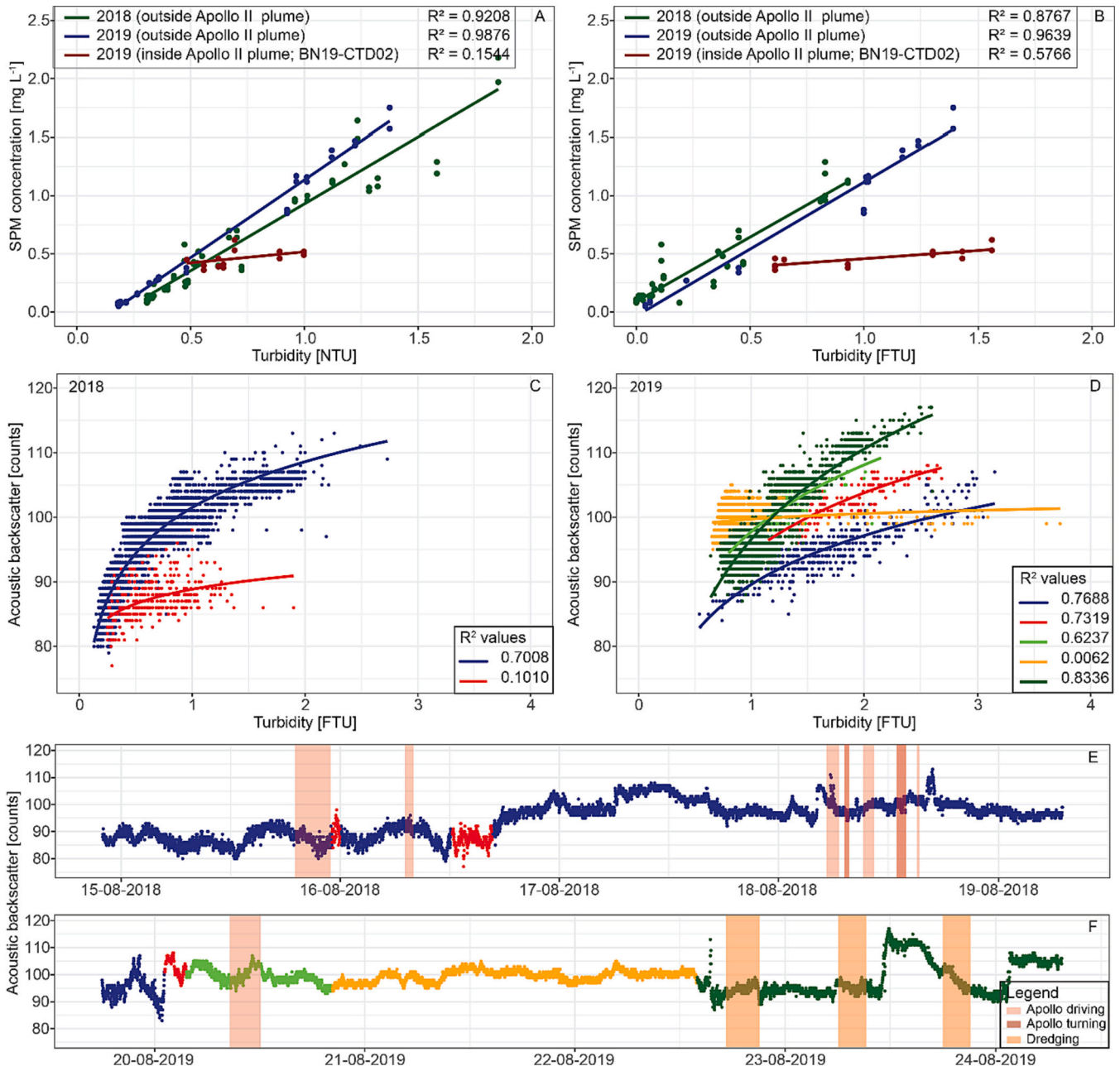

Fig. 9. Relationship between SPM mass concentration, optical backscatter and acoustic backscatter. A and B) SPM mass concentration measured by filtration of Niskin water samples vs. turbidity measured simultaneously with WetLabs OBS (A) and JFE Advantech OBS (B). Green and blue data points represent background samples collected from outside the plume. Red data points represent samples collected from the *Apollo II* plume (BN19-CTD02). C and D) Acoustic backscatter recorded with Nortek Aquadopp at 3 mab vs. turbidity measured simultaneously with JFE Advantech OBS at 3 mab in, respectively, BN18-M1 (C) and mooring BN19-M1 (D). The different colours represent particle populations with different optical-acoustic characteristics, occurring at different time intervals in 2018 and 2019, as respectively shown in E and F. The shaded bars in E and F represent the times *Apollo II* was driving or turning (red), and when the dredging took place (orange). (For interpretation of the references to colour in this figure legend, the reader is referred to the web version of this article.)

confirmed by diving ROV *Zonnebloem* into and out of the plume while following *Apollo II* (Fig. 8D).

Tow-yo-ing the CTD through the *Apollo II* sediment plume with the LISST-200X in-situ particle size analyser mounted within the lower part of the frame gave insight into the contrasting particle size distributions of the *Apollo II* plume (enhanced beam attenuation) compared to background turbidity levels, especially in BN18-CTD19 (Fig. 7A and Supplement Fig. 4A and B). Especially in BN18-CTD19, this is well illustrated, with particle size distributions in the *Apollo II* plume dominated by very small particles with a broad and flat mode centred around 25 μm, comparable to the fine particle size mode observed in the surface sediment. In the background water, there was a dominance of larger particles with a pronounced mode centred around 250 μm, similar to what was seen in the LISST records of 2019.

4.6. Plume dispersion

During the 2018 field test, *Apollo II* made an unsuccessful first attempt to drive along the mooring array on August 16th, but on August 18th, two complete lines of 1000 m at approximately 100 and 150 m distance from the single-line mooring array, and a third incomplete line at 250 m distance (Fig. 1; Supplement Fig. 2) were driven.

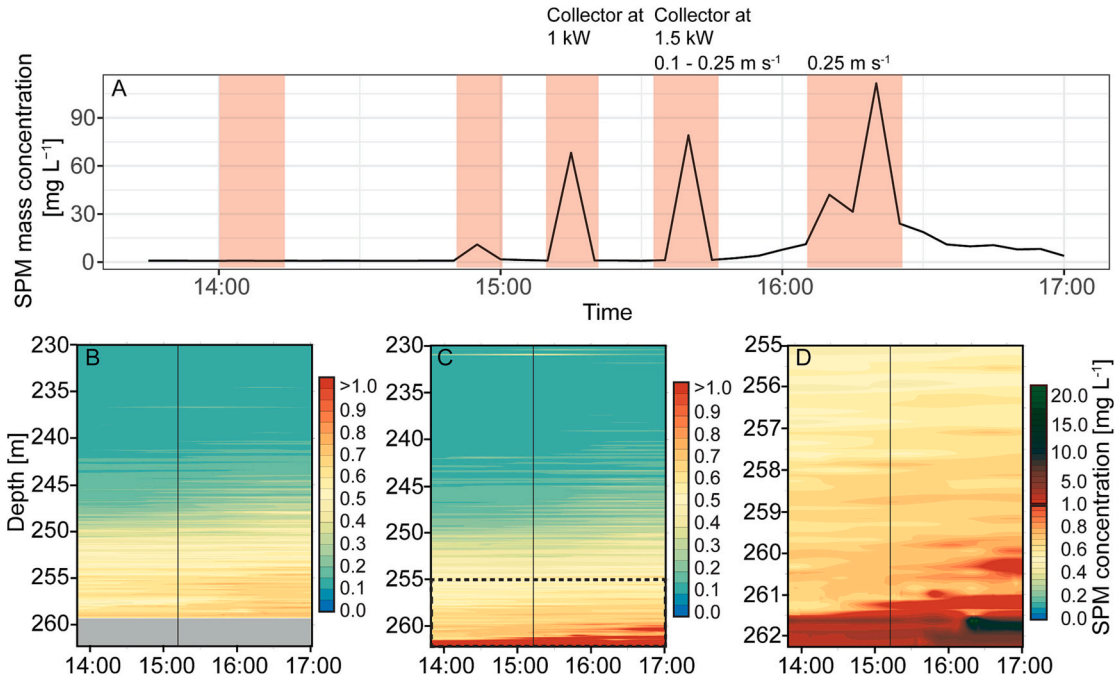

Fig. 10. Time series of SPM mass concentration recorded in the wake of *Apollo II* while the vehicle was driving over the seabed on 12 August 2018. A) SPM mass concentration recorded by a JFE OBS mounted at the rear of *Apollo II*. Shaded areas mark intervals when *Apollo II* was driving over the seabed, stepwise increasing forward speed, and power of the hydraulic collector pump. B—D) SPM mass concentration recorded by JFE OBSs mounted on the CTD, operated in tow-yo mode while the ship was following *Apollo II*. Vertical black line marks the time when the hydraulic collector of *Apollo II* was switched on. B) was recorded by the JFE OBS mounted at the base of the CTD-frame which was lowered until 4 mab, thereby remaining just above the plume. C) was recorded by the OBS suspended 3 m below the CTD-frame, which reached until 1 mab and thereby dipped into the plume. D) same as C), showing the lowest 8 m to the seabed.

Unfortunately, due to issues with the pump of the hydraulic collector, only the plume generated by the propulsion of the vehicle was recorded by the moored sensors. Furthermore, due to a malfunctioning compass, navigation of the vehicle was done based on USBL-tracked position, which resulted in a path that was far from straight. What makes interpretation of the recorded plume data even more challenging is the variable bottom current direction. While *Apollo II* was driving its first line at 100 m from the moorings, the current was directed towards the SW, carrying the plume towards the mooring array (Fig. 11). However, while the vehicle was making the turn to start driving the second line at 150 m from the moorings, the current had changed direction to NW and N, carrying the plume parallel to or even away from the mooring array. In the following hours the current changed further to NE and then to SE, and it was only after *Apollo II* had come to a halt in the middle of the third line at 250 m from the moorings that the current turned again to SW and carried the plume towards the moorings. The succession of events is readily recognised in the time series of SPM mass concentration recorded by the OBSs at 1 and 3 mab (Fig. 11B). The plume produced in the first line showed in the OBS at 1 mab as a sharp increase in SPM mass concentration from about 1.5 to over 6 mg L^{-1}. Only a very weak trace of the plume was recorded by the OBS at 3 mab, confirming what was observed in the CTD tow-yo casts that the plume in its initial phase hardly extended higher than 2 mab. The plume produced in the third line was recorded with some delay in time by the OBS at 1 mab, with a distinct rise in SPM mass concentration from about 1.5 to almost 4 mg L^{-1}. This time, the plume was also clearly recorded by the OBS at 3 mab.

During the 2019 field test, on August 20th, the *Apollo II* drove one line of 1000 m at 50 m distance from the mooring array (Fig. 1; Supplement Fig. 2) with the hydraulic nodule collector switched on. With the compass working properly, the driven path was impeccably straight this time. Unfortunately, technical issues forced the vehicle to a full stop shortly after starting the second track line at 60 m distance. Considering the current velocity data recorded by the moored current profilers, the timing for driving the first line was not well chosen. When *Apollo II* started driving the first line at 08:01 UTC, the near-bed current was directed NE, carrying the plume away from the mooring array (Fig. 12 BN19-M3). Only after 11:00 UTC the current turned to SW, now carrying the plume towards the moorings. In the front line of the mooring array, 50 m away from the path of *Apollo II* (moorings BN19-M1 to BN19-M4), the sediment plume was mainly recorded by sensors at 1 mab, with SPM mass concentrations going up to 5 mg L^{-1}. Approximately one hour later the plume arrived at BN19-M5, 200 m away from the path of *Apollo II*. Here, the SPM mass concentration was higher when compared to the moorings BN19-M1 to BN19-M4, going up to 6 mg L^{-1} at 1 mab and 3 mg L^{-1} at 3 mab. Another 45 min later the plume was also recorded at BN19-M6, 350 m away from the path of *Apollo II* with SPM mass concentrations of 3.5 mg L^{-1} and 2.5 mg L^{-1} at 1 and 3 mab, respectively. The two moorings equipped with sediment traps, sampled settling particles during the *Apollo* II drive-by on the 20th of August. The recorded mass fluxes varied between 200 and 800 mg m^{-2} h^{-1} (Supplement Fig. 5). Highest mass fluxes were recorded between 11:45–12:45 UTC and 12:00–13:00 UTC at BN19-M4 and BN19-M5, respectively. While the maximum flux at BN19-M5 coincided with the time the plume passed by the maximum at BN19-M4 occurred only after the plume had passed.

After technical issues had stopped further testing of *Apollo II* in 2019, a plume was generated on 22 and 23 August by means of a steel beam with trailing lengths of chain, which was towed repeatedly over the seabed parallel to the mooring array, at distances of 50 to 180 m. However, even when the current was carrying the plume directly towards the moorings, maximum recorded SPM mass concentrations did not exceed 2.5 mg L^{-1}, apart from some short-lived increases in SPM mass concentration on 22 August 2019, which were hard to distinguish against the variable background SPM mass concentration (Fig. 6).

5. Discussion

Environmental management of deep-sea mining activities requires

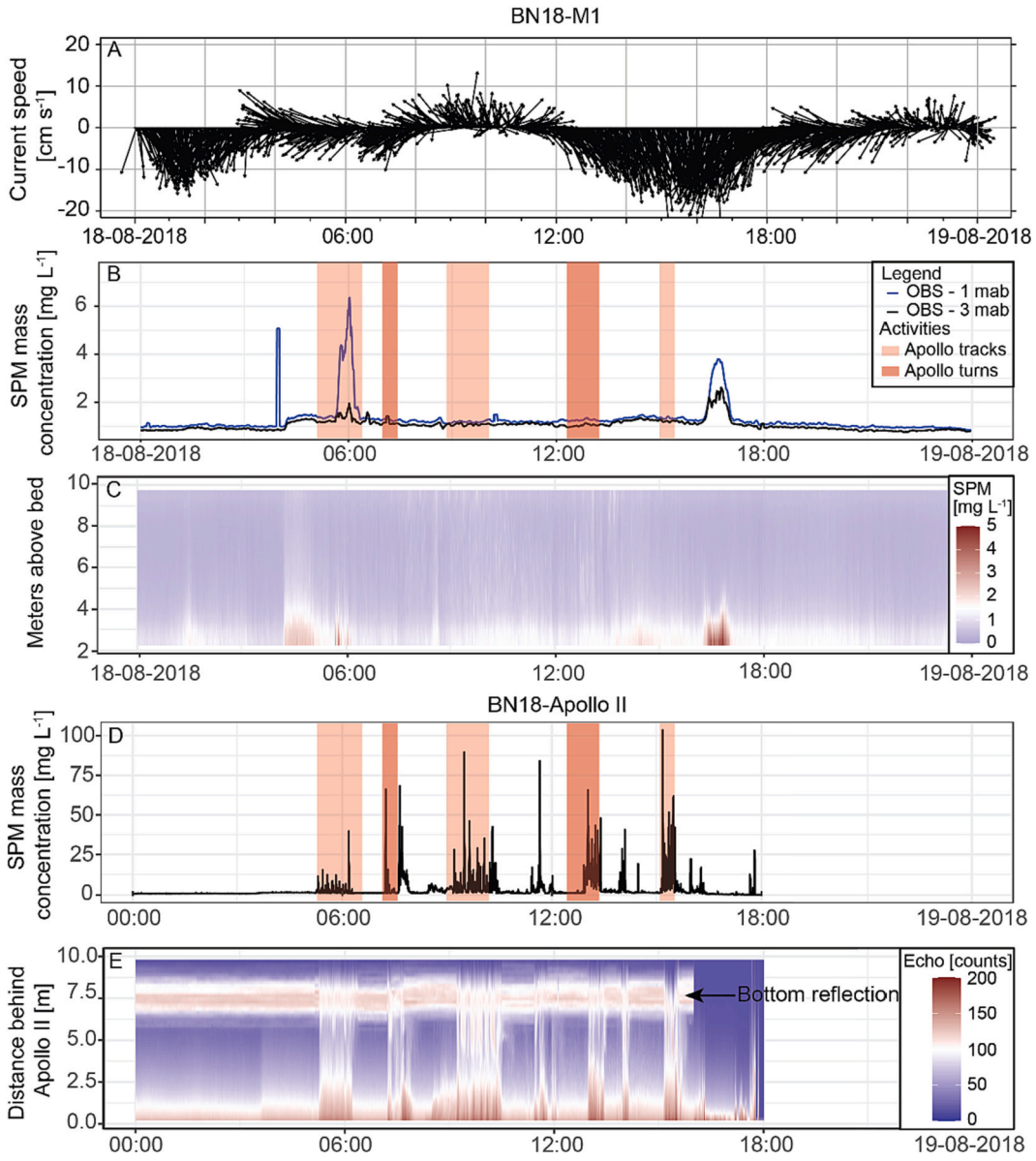

Fig. 11. SPM mass concentration and current speed and direction recorded during the *Apollo II* drive-by experiment on 18 August 2018. A) Near-bottom current speed and direction recorded at 2 mab by the 2 MHz Nortek Aquadopp on mooring BN18-M1. B) SPM mass concentration recorded by the JFE OBSs at 1 mab (dark blue) and 3 mab (black) on mooring BN18-M1. Shaded areas mark intervals when *Apollo II* was driving over the seabed. C) Vertical profile of SPM mass concentration as converted from recorded acoustic backscatter by the Nortek Aquadopp on mooring BN18-M1. For conversion procedure see Supplementary Fig. 6. D) SPM mass concentration recorded by the JFE OBS mounted at the rear of *Apollo II*. E) Profile of acoustic backscatter (raw counts) recorded by the Nortek Aquadopp profiler mounted facing backwards at the rear of *Apollo II*. The strong reflection at 7.5 m distance is produced by impingement of the acoustic beam with the seabed. The abrupt end of the bottom reflection at 15:33 indicates that the vehicle tilted sideways at that point. Details of experimental configuration are provided in Supplementary Fig. 2. (For interpretation of the references to colour in this figure legend, the reader is referred to the web version of this article.)

monitoring designs and strategies that are capable of reliably assessing the impact of ongoing mining operations relative to a pre-mining baseline (Jones et al., 2020). In addition, sediment plumes may cause delayed changes to the system, resulting in disturbances far beyond the mining site, in otherwise pristine and undisturbed deep-sea regions (Gardner et al., 2018; Jones et al., 2020). Environmental monitoring of sediment plumes should thus address both physical drivers (currents and their variability) as well as plume response (horizontal and vertical propagation and settling) at different spatial and temporal scales. In this study, we presented different experimental approaches for monitoring sediment plumes which we tried out during two deep-sea mining field tests in the Alboran Sea (western Mediterranean). The adopted designs consisted of both moving, vessel-based, operations (S-ADCP, CTD, ROV, crawler-mounted sensors), and sampling with a static sensor array for measurements of water column and near-bottom currents, sediment characteristics and plume evolution and propagation. Based on our experiences as summarised in the previous section, we will discuss the merits and shortcomings of these designs.

5.1. Environmental setting of the field test

Prior to the field tests of the *Apollo II* scaled mining vehicle in 2018 and 2019, various components of the propulsion system and the hydraulic collector had already been tested extensively in a lab environment, submerged in a test tank filled with fresh water and on a substrate composed of fine sand or a mixture of sand and clay (Lucieer et al., 2017). With water and sediment characteristics very different from those encountered in prospected mining sites in the deep sea, the lab

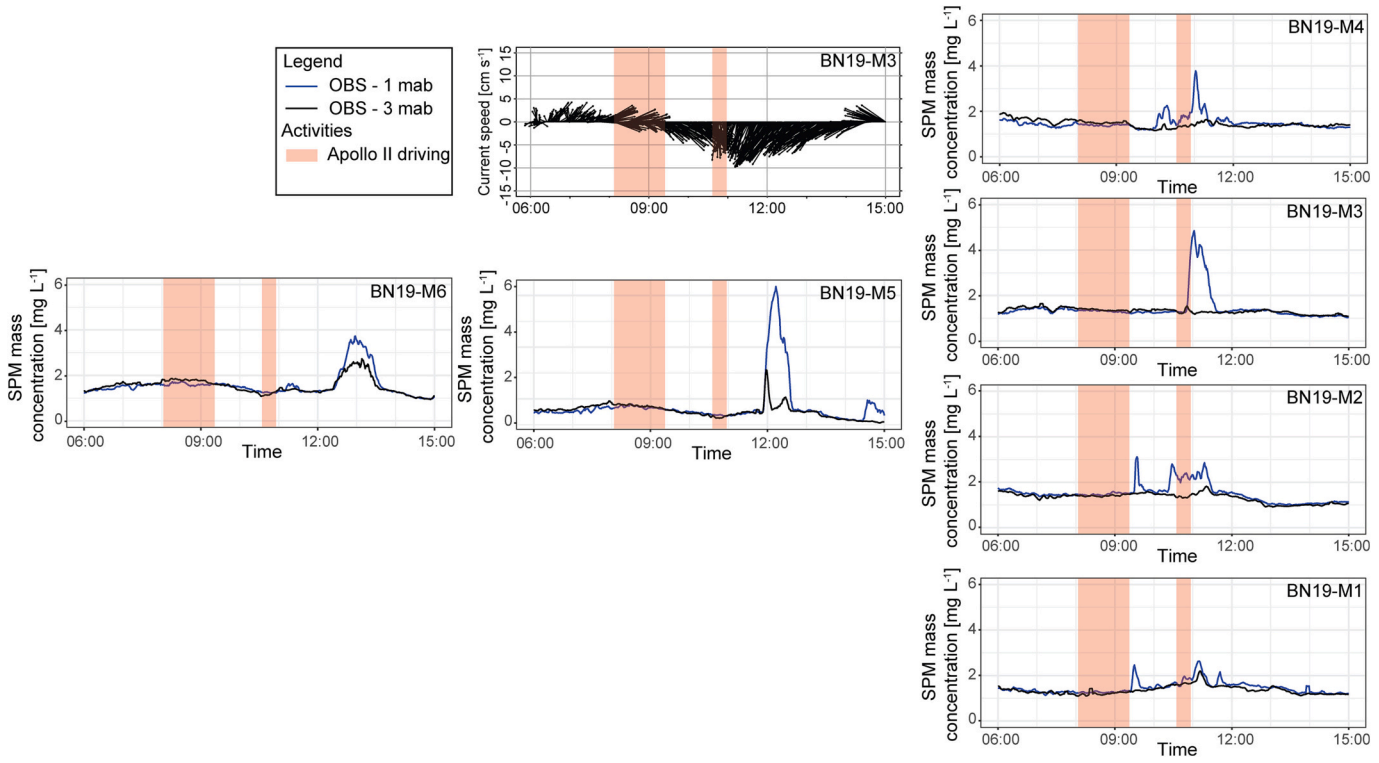

Fig. 12. SPM mass concentration and current speed and direction recorded with JFE OBS and Nortek Aquadopp on moorings BN19-M1 to M6 during the *Apollo II* drive-by experiment on 20 August 2019. SPM mass concentration recorded at 1 mab and at 3 mab is indicated with blue and black line, respectively. Shaded areas mark intervals when *Apollo II* was driving over the seabed. Details of the experimental configuration are provided in Supplementary Fig. 2. (For interpretation of the references to colour in this figure legend, the reader is referred to the web version of this article.)

results have little value for predicting environmental effects arising when the mining equipment is used in a deep-sea setting. In addition, the test tank offered very limited space for experimenting with a realistic plume monitoring setup. The test area in Málaga Bight, despite of its relatively shallow water depth, offered all the space needed, and a seabed and water column that for a number of relevant aspects provided a good approximation of a deep-sea mining setting.

The weakly sloping seabed covered with soft, muddy sediment provided a good analogy for the abyssal seabed for which the mining is designed. Absence of nodules was the most important 'shortcoming' of the Málaga Bight seabed from a testing perspective, but lab tests of the hydraulic collector had already yielded very satisfying results. For assessment of the sediment plume stirred up by the vehicle, it was more important that the sediment of the Málaga Bight seabed was predominantly composed of clay and silt, which are also the dominant fractions in surface sediment in polymetallic nodule fields of the Pacific Ocean (e.g. BGR Bundanstalt für Geowissenschaften und Rohstoffe, 2018).

The prevalence of fine-grained sediment in the test area, atypical for a relatively shallow near-coast environment, reflects the overall weak bottom current regime in the Málaga Bight. The sluggish current regime in turn is the result of the absence of strong tides in the Mediterranean Basin and the relative shelter in the bight provided by mountainous headlands protruding from the coast. Weak near-bed currents, with magnitude mostly below 10 cm s^{-1} and of a variable direction, in combination with a weak density stratification, provide a good analogy for the hydrodynamic regime found in the abyssal ocean.

The variable tidal current, however, posed a considerable challenge with regards to timing of our drive-by experiments. With improper timing, the plume generated by the test vehicle would drift away from our moored sensors, and in the best case was recorded only hours later when the current had turned to a more favourable direction. In the time span between generation and detection of the plume, a considerable part of the suspended sediment must have settled out and have been diluted by mixing with ambient non-plume water, as reflected by the relatively low SPM mass concentrations recorded by the moored sensors. Therefore, we used our S-ADCP data, available in real time and processed and analysed on a daily basis, to find the optimal time window for conducting our drive-by experiment. Post-hoc comparison with current data recorded by our moored current profilers revealed that changes in current direction at 3 m above the seabed typically lagged 1–2 h behind (Fig. 5D, E) those observed at 25 m and higher above the seabed by the S-ADCP. This can be attributed to the phase shift of the baroclinic tidal current indicating strong vertical shear as a result of Ekman veering in the bottom boundary layer (Perlin et al., 2007). As a result, we started the drive-bys while the currents were still directed away from the moorings, so that we failed to record the plume while it was freshly produced. This initial mismatch in timing would have been compensated if the following lines had been successful, and the current would have carried the plume straight towards the moorings. The challenges posed by variable currents are similarly present in a deep-sea setting, as found in small-scale plume experiments conducted in the abyssal Pacific (DISCOL Experimental Area, Baeye et al., 2022; CCZ, Haalboom et al., 2022; Purkiani et al., 2021). In a future monitoring scenario, it would be advantageous to have near-bottom current data from the mining site in real time, to feed into an operational plume dispersion model.

An aspect in which the bottom water of Málaga Bight was markedly different from that of the typical abyssal ocean setting was in its high and highly variable background SPM mass concentration. Recorded intervals of increased background SPM mass concentration, as shown in Fig. 6A and C, did not seem to correlate with periods of increased current speed, precluding sediment resuspension by bottom currents as their cause. A correlation was not found either with the diel migration of pelagic fauna to deep water during daytime, or with ship-based sampling activities that might have stirred up sediment from the seabed. The most likely explanation for the variable turbidity seems to be nearby trawling activity. Whilst fishing vessels operating in the area kept a

minimum distance of 1 nautical mile to RV *Sarmiento de Gamboa* and the moorings, the plumes produced by trawling may well have drifted towards our moorings in a few hours' time. Interference by bottom trawling or other human activity is not an issue in the polymetallic nodule fields in the abyssal Pacific Ocean, where background SPM mass concentration is typically on the order of 0.01 mg L^{-1} (Lal, 1977; Haalboom et al., 2022). Despite indications that bottom currents in this area are periodically enhanced under influence of mesoscale eddies passing by in the surface ocean layer (Aleynik et al., 2017), there are no records yet that these lead to substantial sediment resuspension. Different from Málaga Bight, where the more distal plume produced by *Apollo II* could not be distinguished from background turbidity, any resuspension of sediment in the deep sea will be readily detected and will be traceable to considerable distance away from the source.

5.2. Operational settings of mining machinery

The trials with *Apollo II* involved testing of different functions of the vehicle in the field, including driving performance at different speeds, and performance of the hydraulic collector at different settings (i.e. pump rate of the collector pump and stand-off distance of the collector relative to the seabed). Whilst the technical validation was overall successful, the environmental testing was flawed by a lack of replication due to both technical issues and the inherent variability of the environment. Due to the failing compass, driving straight lines at constant speed turned out problematic in 2018, and due to the untimely failure of the hydraulic collector pump only the plume produced by the motion of the vehicle could be observed. In 2019 the hydraulic collector pump worked properly, but there was no good control of the standoff distance of the collector to the seabed. As a result, the collector merely grazed the sediment surface. Our data may thus give a more positive impression of the resulting environmental pressures than when the mining vehicle would have operated with the hydraulic collector on full power and driving at its desired speed. For any future monitoring of deep-sea mining, it seems important that basic operational parameters such as underwater position, driving speed, and collector performance will be continuously logged. In addition, it would also be desirable that plume emission from the diffuser and the plume produced by the propulsion of the vehicle are measured directly, as a source term for operational modelling of plume dispersion, but also to allow a standardised evaluation of the environmental performance of mining gear (Weaver et al., 2022). Our measurement of suspended sediment concentration at the exit of the diffuser, even when not conclusive as the sensors were not located directly in the diffuser flow, showed the feasibility of this approach.

5.3. Setup of the plume monitoring array

Our plume monitoring setup, with sensors mounted on the mining vehicle and moored on the seabed at set distances from the source, proved effective to record the progressive spreading of the plume under influence of currents and turbulent mixing, as well as the decrease in SPM mass concentration within the plume resulting from dilution with ambient water and settling out of sediment particles. Even with the variable background SPM mass concentrations, the passage of the plume at different sensor locations within a radius of a few hundred metres from the source was noted by a distinct increase in SPM mass concentration. The recorded data on current velocity and SPM mass concentration would in principle be good for validation and calibration of a numerical model describing the overall dispersion and redeposition of sediment resuspended by the mining vehicle, including in places where no sensor data are available.

Placement of sensors close to the source would be desirable to better constrain the initial concentration and dispersion of the sediment plume. In our experimental setup with moorings, where anchor positions were accurately determined and top floats were clearly visible at the sea surface, 50 m was deemed the absolute minimum for safely driving by with *Apollo II* tethered to the ship. The need for caution was demonstrated by the failed first drive-by on 16 August 2018, when the umbilical of *Apollo II* accidentally crossed one of the mooring lines. The problems involved in the use of mooring lines could be overcome by positioning sensors directly on the seabed by means of an ROV. This approach proved successful in a dredge plume experiment carried out in 2019 in the CCZ (Purkiani et al., 2021; Haalboom et al., 2022), but here a working class deep-sea ROV with extended capacity for handling equipment was available. The small ROV *Zonnebloem* which we used in our experiment in Málaga Bight was more limited in that respect, while finding back equipment might also have been problematic with the sometimes poor visibility near the bottom. The safest option for near-field plume monitoring after all seems to be to mount acoustic profilers directly on the mining vehicle, with beams directed both backwards and sideways. Results from using one of the 2 MHz Aquadopp profilers for that purpose seem promising (Fig. 11C), but a proper calibration of the acoustic backscatter signal received over the full distance range of >10 m would be essential for conversion of the acoustic signal to SPM mass concentration. At high suspended sediment concentration near the source, sound absorption by suspended sediment may prove to be a factor that needs to be accounted for (Lohrmann, 2001).

For monitoring the more distal plume, our moored sensor layout proved effective. Especially by the combination of acoustic devices, recording vertical profiles of acoustic backscatter extending to >10 m above the seabed, and optical backscatter sensors, which are relatively straightforward to calibrate, and which allow cross-calibration of the acoustic backscatter signal. Both the optical and acoustic devices confirmed what was also observed with the CTD and ROV, that the plume initially stayed very close to the seabed (Fig. 10C and D), and only with progress of time and distance from the source extended higher above the seabed, while at the same time developing a clear vertical gradient in concentration (Fig. 12). Although sensors could have been placed even closer to the seabed, attached directly to the mooring weights, we chose not to do so to avoid damage to the sensors. We might also have reduced the blind spot in acoustic profiles in the lower 2 mab, resulting from the minimum height of the sensor head at 1.5 mab plus the 0.5 m blanking interval above the sensor head, by mounting the Aquadopp profilers at 10 mab facing downwards. However, in that configuration the most important lower part of the profile close to the seabed would be covered by the more distant depth bins of the profiler, where data may be less reliable and could be influenced by backscatter from the seabed.

The choice to have moorings only on one side of the path driven by *Apollo II* was mainly motivated by the available amount of sensors and mooring equipment. Safe navigation of the ship with tethered *Apollo II* was an additional argument for not placing moorings on both sides of the path. With the good underwater navigation, as achieved in 2019, a drive-through approach might have been an option though, which would have provided good data at times that the current carried the plume away from the main line of moorings. Compared to our single line mooring setup of 2018, our setup of 2019 was significantly improved by the addition of two moorings behind and perpendicular to the first line of moorings, as these additional moorings provided synoptic recordings of the evolution of the plume as it dispersed away from the source. In 2018, insight in the spatial evolution of plume was obtained by driving the vehicle at different distances upstream from the mooring array. In practice, however, the changing tidal currents complicated the comparison of recorded data from consecutive lines.

In view of the rapid decrease in SPM mass concentration in the plume with time and distance to the source, until the point that the plume could no longer be distinguished from the variable background, it seems that a further expansion of the sensor array over distances greater than a few hundred metres from the source would not have had added value. In a deep-sea setting, where bottom waters have a two orders of magnitude lower background SPM mass concentration (e.g. Lal, 1977), a

monitoring array may be spread out over longer distances and still be able to detect the plume. This may even be required in an operational scenario where sensors must be placed at sufficient distance from the mining vehicle without the risk of being overrun.

5.4. Mobile sensor platforms

Compared to the moored sensors, from which the recorded data could be accessed only after recovery, the standard ship-based CTD-Rosette system offered the advantage that vertical profiles of turbidity and other water column characteristics could be investigated in real-time, and that water samples could be collected at any desired moment by firing Niskin bottles. The CTD frame also offered space for mounting additional sensors such as the LISST for in-situ particle sizing. An obvious limitation of operating the CTD-Rosette system from the same ship also used as platform for operating the mining machine was that the plume could only be accessed when currents and navigation of ship and mining machine brought the plume directly below the ship. In practice, with the ship following behind the mining vehicle and at a speed usually higher than the speed of near-bottom currents, it was actually not uncommon that the plume was in reach of the CTD. A more important limitation which we noted was that the CTD could often not be lowered sufficiently close to the seabed to properly sample the low-lying plume. In 300 m water depth, under optimal seastate conditions, and with a very smooth and gently sloping seabed and reliable altimeter on the CTD, we could confidently approach the seafloor to as low as 2 mab. However, even under such ideal conditions, the sensors mounted within the CTD frame and the vertically mounted Niskin bottles would often only graze the very top of the plume. With sensors suspended below the CTD frame, we could reach deeper into the plume, but at the risk of damage to the sensors and erroneous readings in case the sensors would accidentally hit the seabed. In deep-sea settings the minimum distance of safe approach to the seabed is usually held at 5 m, depending on seastate, obviously too far to sample a low-lying plume with sensors and Niskin bottles. A ROV, as shown in our field tests, offers a greater flexibility than a ship-operating CTD-Rosette system in exploring sediment plumes in the vertical and horizontal dimension. With ROV video cameras, the plume can be observed in real-time, and within certain limits of weight and size additional sensors can be added to its payload. Care should be taken, however, that the ROV is not stirring up its own sediment plume. An example of a plume produced by the ROV may be seen in Fig. 6C on the 22nd of August, where we observed an increase in the turbidity at 1 mab shortly after the deployment of the ROV. Tether length and risk of entanglement with the mining vehicle's umbilical and riser system remain limitations for use of a ROV in an operational setting. In that respect, autonomous underwater vehicles (AUV) might seem the most promising technology for operational plume monitoring purposes, as they autonomously can cover relatively large distances on the order of tens of kilometres, and therefore can follow plumes from near field to far field. The required minimum safe flying height above seabed may pose limitations to detection of low-lying plumes with optical backscatter sensors, but this limitation may be overcome by use of downward-looking acoustic profiling devices with appropriate frequency to detect fine-grained suspended sediment.

5.5. Sediment deposition from the plume

Whereas assessment of blanketing of the seabed by sediment deposition from the plume should be an integral part in monitoring of deep-sea mining impact, our experiment was not successful in this respect. The sediment traps in the mooring array appeared not very effective in sampling sediment deposition from the plume, as their opening at 2.5 mab, the lowest we could possibly mount them, was still too high above the seabed to sample the low-lying plume. The observed variation in settling particle flux in the traps could not be unambiguously correlated with the passage of the sediment plume. If placed at a greater distance from the source, where the plume might rise higher, the traps would still only catch deposition from the upper, most dilute, part of the plume. In plume dispersion experiments in the deep Pacific Ocean (Thiel, 2001; Peukert et al., 2018; Haalboom et al., 2022), the areal distribution and thickness of redeposited sediment was assessed from seabed imagery. However, in these experiments, the dark-coloured polymetallic nodules provided a suitably contrasting background against which resettled plume sediment could be readily distinguished. Such optical contrast was not present in our study area, and besides that, it would have been impossible to distinguish sediment settled out from the *Apollo II* plume from sediment settled out from plumes produced by nearby trawling.

5.6. Conversion of optical backscatter to SPM mass concentration

As demonstrated by our field tests, suspended sediment plumes in deep waters can be reliably detected with both optical and acoustic sensors that record the presence of particles by variation in transmitted, diffracted, or backscattered light or sound. For a quantitative assessment of the mass of sediment dispersed through sediment plumes, optical and acoustic sensor data must be converted to a common unit of dry weight of solids per volume of water. Since the amount of transmission, refraction or backscatter of light or sound depends not only on the concentration of particles in suspension but also on physical characteristics of the particles such as their size distribution, relative density and reflectively (e.g. Baker and Lavelle, 1984; Hatcher et al., 2001; Downing, 2006), there is not a single universally applicable function to do the conversion. The conversion should be made on a case-by-case basis through a function appropriate for the specific suspension under investigation. This was clearly illustrated by CTD02 of 2019, the only CTD cast in which we managed to collect water samples from the plume of *Apollo II*. In this cast we found a relationship between optical backscatter and SPM mass concentration notably different from that found in other CTD casts which only sampled background water (Fig. 9). Data obtained with the LISST-200X particle sizer mounted on the CTD demonstrated that dominant particle size within the plume at short range from *Apollo II* was substantially smaller than in the background water outside the plume (Fig. 7A). In the freshly mobilised plume, the size distribution of suspended particles appeared to correspond closely with that of the fine fraction of the surface sediment. The much larger particles that dominated in the background water were likely aggregates composed of aggregated fine-grained mineral and organic matter. The difference in dominant particles sizes in plume and background waters may well explain the different relationship between optical backscatter and SPM mass concentration which we observed for fresh plume and background water. As demonstrated by lab experiments and field observations, fine-grained particles have a larger backscattering surface per unit mass than coarser-grained particles, and hence also produce a higher backscatter response than coarser particles (e.g. Downing, 2006). After the initial mobilisation and dispersion of the fine-grained surface sediment by the action of the mining vehicle, the fine-fraction primary particles are likely to aggregate rapidly into larger particles, by electrostatic attraction of clay particles and probably also favoured by organic material relatively abundant in the near-coast environment. Both field observations in man-made sediment plumes (Durrieu de Madron et al., 2005) and lab experiments (Gillard et al., 2019) demonstrated that aggregation of primary particles of a few μm to tens of μm into larger aggregates of hundreds of μm may occur in a matter of hours.

In this study we have used the regression lines of the majority of samples taken outside the plume to convert all OBS turbidity readings from both the 2018 and the 2019 cruises to SPM mass concentration. We consider the number of samples from within the generated *Apollo II* plume insufficient to establish a reliable conversion specifically for the plume. As a consequence, the SPM mass concentrations reported in this study for the *Apollo II* plume may well be overestimated. As an alternative to our approach of in-situ sensor calibration, sensors could be

calibrated on-board or in the lab with suspensions produced with local surface sediment and bottom water, as described by e.g. Guillen et al. (2000). This seems a valid approach for dredging and deep-sea mining sediment plumes formed by resuspension of surface sediment, but only if the composition of the material in the plume corresponds with that of the surface sediment. In our case in Málaga Bight the seabed contained a substantial fraction of sandy material, which in a field setting will settle out in a matter of minutes after being brought in suspension according to Stokes' Law, but in a lab calibration setting with continuous stirring will be kept in suspension and thus add to the SPM mass concentration. In this case, using a lab-based conversion function for calculating SPM mass concentration from optical backscatter measured in the field will lead to overestimation of the SPM mass concentration. In the typical polymetallic nodule setting where the sediment is predominantly fine-grained and sand represents only a very minor fraction, lab-based sensor calibration may be a good practice. Especially since in-situ calibration of sensors in deep water may be even more difficult than what we experienced in Málaga Bight. However, using a lab-based conversion function for assessing SPM mass concentration in sediment plumes does not account for the effect that particle aggregation may have on optical backscatter. For a monitoring set-up it would therefore be recommended to record not only turbidity but also the particle size at different distances away from the disturbance site.

5.7. Conversion of acoustic backscatter to SPM mass concentration

Conversion of the acoustic backscatter signal from acoustic profilers to SPM mass concentration, on the basis of the logarithmic relationship found between echo level and SPM mass concentration derived from simultaneously recorded optical backscatter data, has been previously employed in field studies (e.g. Durrieu de Madron et al., 2005; Tessier et al., 2008; Mengual et al., 2016). As explained in Haalboom et al. (2021), the acoustic backscatter signal, much like what is described above for the optical backscatter, is not only determined by particle concentration but also by the size of the suspended particles. Following hydroacoustic theory as presented in Haalboom et al. (2021), the Nortek Aquadopp 2 MHz profilers which we used in our plume monitoring experiment have a lower detection limit for particles of 12 μm diameter, and maximum sensitivity for particles of 242 μm diameter. These particle sizes are close to what we found, respectively, as fine-grained mode in surface sediment, and as coarse-grained mode of suspended particles in background water as recorded by the LISST-200X. It may thus be expected that different states of particle aggregation occurring in the *Apollo II* sediment plume and in background water would be reflected by different intensities of acoustic backscatter. Sediment freshly mobilised and dispersed by *Apollo II*, forming an unaggregated suspension, would produce a lower acoustic backscatter than the suspension in a more advanced state where the primary sediment particles would have aggregated into larger-sized particles. This would explain the occurrence of the two data clusters observed in the plot of echo level vs. SPM mass concentration for mooring BN18-M1 (Fig. 9). It appears puzzling, however, that similar data clusters with low acoustic backscatter were not found associated with other time intervals when *Apollo II* was active near the moorings. Possibly the higher and variable background SPM mass concentration at those times masked the signature of the fresh *Apollo II* plume, or the *Apollo II* plume might itself already have evolved to a more aggregated state. Also, the suspended particles present in trawling plumes advected from adjacent areas, here considered as background to the *Apollo II* plume signal, may also have been in variable states of aggregation. The LISST-200X data recorded in 2019, showing considerable variability in particle size distribution in the background water (Fig. 7A and Supplement Fig. 4), seem to confirm this. In view of the variable relationship between acoustic backscatter and SPM mass concentration, illustrated by the different data clusters in Fig. 9, caution seems to be due when using acoustic backscatter for deriving SPM mass concentration. Even so, this approach may give valuable insight in gradients of SPM mass concentration within mining plumes.

6. Concluding remarks – Application to deep-sea mining setting

Plume monitoring in a realistic industrial mining scenario is challenging, when considering the temporal (years to decades) and spatial (hundreds of kilometres) scales, over which measurements and maintenance of instruments may need to be realised. Recent studies have highlighted the importance of smaller-scale experiments for developing mining-related plume monitoring strategies at a time, where deep-sea mining at an industrial scale is waiting in the wings. Monitoring data obtained in the field are essential for validation and calibration of numerical models of plume dispersion. Conversely, numerical models help to better understand monitoring results, and help to identify data gaps. Our own experimental monitoring efforts, even though performed in a relatively shallow marine setting, confirm that robust monitoring can be achieved by combining standard commercial instrumentation on suitable stationary and moving platforms. Most of the monitoring methods presented in this study can be applied also in a deep-sea setting, although sometimes in an adapted form.

- A good control on the plume source, i.e., when and where sediment is being mobilised by the mining machine and the rate of sediment mobilisation and discharge, is important for interpretation of far field sensor recordings, and is essential for numerical modelling of plume dispersion.
- The initial SPM mass concentration of the plume discharged from the mining vehicle may be derived from operational data on navigation of the mining vehicle and erosion depth and pumping rate of the collector but should preferably also be measured directly by sensors mounted on the mining vehicle.
- To allow detection of the low-lying plume in its initial stage near the source, it is important that at least some sensors are placed very close to the seabed. High-frequency acoustic profilers moored close to the seabed in combination with calibrated OBSs are suitable for measuring vertical profiles of suspended sediment concentration above the seabed.
- Mobile sensor platforms like the standard CTD-Rosette system deployed from a ship are limited in the distance to which they can safely approach the seabed, and for that reason are prone to miss the initial low-lying plume. The same limitation applies when AUVs are employed for plume monitoring. The lower metres of water column directly above the seabed could, however, be in range for a downward-looking high-frequency acoustic profiler.
- Current velocities close to the seabed measured with moored high-frequency current profilers differed substantially from velocities measured higher up in the water column with ship-ADCP and long-range moored ADCP. For predicting the initial dispersion of the sediment plume, near-bottom current velocity records should be used.
- Turbidity sensors used for plume monitoring need to be calibrated in-situ by reference to simultaneously collected samples of SPM or in a lab setting using suspensions made from local surface sediment. However, particle aggregation occurring in the sediment plume may affect the optical and acoustic backscatter characteristics of the SPM, resulting in under- or overestimation of SPM mass concentration.
- Assessment of particle size distribution in sediment plumes may contribute to more reliable quantification of SPM mass concentration.

Declaration of Competing Interest

The authors declare that they have no known competing financial interests or personal relationships that could have appeared to influence the work reported in this paper.

Data availability

CTD data, S-ADCP data, data collected by the turbidity sensors, LISST-200X, and ADCPs mounted on the CTD-frame, *Apollo II* and moorings, as well as filter weights for SPM sampling and data on particle size analysis of the surface sediments, collected during the cruises in 2018 and 2019 are available in the NIOZ database (https://dataverse.nioz.nl/dataverse/doi) under, respectively, DOI 10.25850/nioz/7b.b.vd and 10.25850/nioz/7b.b.wd.

Acknowledgements

We thank the captains and crew of RV *Sarmiento de Gamboa* for their essential assistance during the two field tests. Technical assistance onboard the ship was provided by Arturo Castellón and his team of the Marine Technology Unit of the Spanish Research Council UTM-CSIC. The ROV team of the Flanders Marine Institute (VLIZ) assisted in the field tests by seabed surveys and plume observations with ROV *Zonnebloem* and supporting underwater navigation with the GAPS system. The engineering team of IHC Mining, responsible for driving Apollo II, played a key role in carrying out the field tests. We thank our colleagues from the NIOZ-EDS department for borrowing their LISST-200X and in particular Dr. Karline Soetaert for her assistance with the processing of the data. This research was funded by the Blue Nodules project (EC grant agreement no. 6887851). HdS, CM and LdJ acknowledge additional funding from the Blue Harvesting project (EIT RM grant no. 18138). We thank three anonymous reviewers for insightful comments and constructive criticism which improved the manuscript.

References

Ainslie, M.A., McColm, J.G., 1998. A simplified formula for viscous and chemical absorption in sea water. J. Acoust. Soc. Am. 103 (3), 1671–1672. https://doi.org/10.1121/1.421258.

Aleynik, D., Inall, M.E., Dale, A., Vink, A., 2017. Impact of remotely generated eddies on plume dispersion at abyssal mining sites in the Pacific. Sci. Rep. 7 (1), 16959. https://doi.org/10.1038/s41598-017-16912-2.

Baeye, M., Purkiani, K., de Stigter, H.C., Gillard, B., Fettweis, M., Greinert, J., 2022. Tidally Driven Dispersion of a Deep-Sea Sediment Plume Originating from Seafloor Disturbance in the DISCOL Area (SE-Pacific Ocean). Geosciences 12, 8. https://doi.org/10.3390/geosciences12010008.

Baker, E.T., Lavelle, J.W., 1984. The effect of particle size on the light attenuation coefficient of natural suspensions. J. Geophys. Res. 89 (C5) https://doi.org/10.1029/JC089iC05p08197.

Baraza, J., Ercilla, G., Lee, H.J., 1992. Geotechnical properties and preliminary assessment of sediment stability on the continental slope of the northwestern Alboran Sea. Geo-Mar. Lett. 12, 150–156. https://doi.org/10.1007/BF02084926.

Bárcenas, P., 2011. Spatial variability of surficial sediment on the northern shelf of the Alboran Sea: the effects of hydrodynamic forcing and supply of sediment by rivers. J. Iber. Geol. 37 (2), 195–214. https://doi.org/10.5209/revJIGE.2011.v37.n2.8.

Barnett, B.G., Suzuki, T., 1997. The use of kriging to estimate resedimentation in the JET experiment. In: Proceedings of the International Symposium on Environmental Studies for Deep-Sea Mining, pp. 143–151.

BGR Bundanstalt für Geowissenschaften und Rohstoffe, 2018. Environmental Impact Assessment 827 for the Testing of a Pre-Protoype Manganese Nodule Collector Vehicle in the Eastern German License 828 Area (Clarion-Clipperton Zone) in the Framework of the European JPI-O MiningImpact 2 Research 829 Project. https://isa.org.jm/minerals/environmental-impact-assessments.

Boschen, R., de Stigter, H.C., Tayman, C., Mravak, Z., 2020. Blue Nodules Deliverable Report D1.7: Environmental Impact Assessment (EIA) component for test mining up to prototype level (TRL 6). https://blue-nodules.eu/download/public_reports/public_reports/Blue-Nodules-688975-D1.7-Report-EIA-Assessment-FINAL.pdf.

Brennan, M., Canals, M., Coleman, D., Austin Jr., J., Amblas, D., 2015. Bathymetric Extent of recent Trawl damage to the Seabed Captured by an ROV Transect in the Alboran Sea. Oceanography 28 (4), 8–10. http://www.jstor.org/stable/24861922.

Brockett, T., Richards, C.Z., 1994. Deep Sea Mining Simulator for Environmental Impact Studies: Sea Technology, pp. 77–82.

Daly, E., Johnson, M.P., Wilson, A.M., Gerritsen, H.D., Kiriakoulakis, K., Allcock, A.L., White, M., 2018. Bottom trawling at Whittard Canyon: evidence for seabed modification, trawl plumes and food source heterogeneity. Prog. Oceanogr. 169, 227–240. https://doi.org/10.1016/j.pocean.2017.12.010.

DEME Group, 2021. https://www.deme-group.com/news/metal-rich-nodules-collected-seabed-during-important-technology-trial.

Downing, J., 2006. Twenty-five years with OBS sensors: the good, the bad, and the ugly. Cont. Shelf Res. 26 (17–18), 2299–2318. https://doi.org/10.1016/j.csr.2006.07.018.

Durrieu de Madron, X., Ferré, B., Le Corre, G., Grenz, C., Conan, P., Pujo-Pay, M., Buscail, R., Bodiot, O., 2005. Trawling-induced resuspension and dispersal of muddy sediments and dissolved elements in the Gulf of Lion (NW Mediterranean). Cont. Shelf Res. 25, 2387–2409.

Ercilla, G., Juan, C., Hernández-Molina, F.J., Bruno, M., Estrada, F., Alonso, B., Casas, D., Farran, M., Llave, E., García, M., Vázquez, J.T., D'Acremont, E., Gorini, C., Palomino, D., Valencia, J., El Moumni, B., Ammar, A., 2016. Significance of bottom currents in deep-sea morphodynamics: an example from the Alboran Sea. Mar. Geol. 378, 157–170. https://doi.org/10.1016/j.margeo.2015.09.007.

Firing, E., Hummon, J.M., 2010. Shipboard ADCP Measurements.

Firing, E., Ranada, J., Caldwell, P., 1995. Processing ADCP Data with the CODAS Software System Version 3.1. Joint Institute for Marine and Atmospheric Research, University of Hawaii & National Oceanographic Data Center.

Gardner, W.D., Richardson, M.J., Mishonov, A.V., 2018. Global assessment of benthic nepheloid layers and linkage with upper ocean dynamics. Earth Planet. Sci. Lett. 482, 126–134. https://doi.org/10.1016/j.epsl.2017.11.008.

Gillard, B., Purkiani, K., Chatzievangelou, D., Vink, A., Iversen, M.H., Thomsen, L., 2019. Physical and hydrodynamic properties of deep sea mining-generated, abyssal sediment plumes in the Clarion Clipperton Fracture Zone (Eastern-Central Pacific). Elem. Sci. Anthropocene. https://doi.org/10.1525/elementa.343 v. 7.

Gjerde, K.M., Reeve, L.L.N., Harden-Davies, H., Ardron, J., Dolan, R., Durussel, C., et al., 2016. Protecting Earth's last conservation frontier: scientific, management and legal priorities for MPAs beyond national boundaries. Aquat. Conserv.: Mar. Freshw. Ecosyst. 26, 45–60. https://doi.org/10.1002/aqc.2646.

Glover, A.G., Smith, C.R., 2003. The deep-sea floor ecosystem: current status and prospects of anthropogenic change by the year 2025. Environ. Conserv. 30 (3), 219–241, 10.101/S0376892903000225.

Gollner, S., Kaiser, S., Menzel, L., Jones, D.O.B., Brown, A., Mestre, N.C., et al., 2017. Resilience of benthic deep-sea fauna to mining activities. Mar. Environ. Res. 129 https://doi.org/10.1016/j.marenvres.2017.04.010, 7 6-101.

Guillen, J., Palanques, A., Puig, P., De Madron, X.D., Nyffeler, F., 2000. Field calibration of optical sensors for measuring suspended sediment concentration in the western Mediterranean. Sci. Mar. 64 (4), 427–435. https://doi.org/10.3989/scimar.2000.64n4427.

Haalboom, S., de Stigter, H., Duineveld, G., van Haren, H., Reichart, G.-J., Mienis, F., 2021. Suspended particulate matter in a submarine canyon (Whittard Canyon, Bay of Biscay, NE Atlantic Ocean): assessment of commonly used instruments to record turbidity. Mar. Geol. 434 https://doi.org/10.1016/j.margeo.2021.106439.

Haalboom, S., Schoening, T., Urban, P., Gazis, I.-Z., de Stigter, H.C., Gillard, B., et al., 2022. Monitoring of anthropogenic sediment plumes in the Clarion-Clipperton Zone, NE equatorial Pacific Ocean. Front. Mar. Sci. – Deep-Sea Environ. Ecol. 9, 882155. https://doi.org/10.3389/fmars.2022.882155.

Hatcher, A., Hill, P., Grant, J., 2001. Optical backscatter of marine flocs. J. Sea Res. 46 (1), 1–12. https://doi.org/10.1016/S1385-1101(01)00066-1.

Hein, J.R., Mizell, K., Koschinsky, A., Conrad, T.A., 2013. Deep-ocean mineral deposits as a source of critical metals for high- and green-technology applications: Comparison with land-based resources. Ore Geol. Rev. 51, 1–14. https://doi.org/10.1016/j.oregeorev.2012.12.0.

Hoagland, P., Beaulieu, S., Tivey, M.A., Eggert, R.G., German, C., Glowka, L., Lin, J., 2010. Deep-sea mining of seafloor massive sulfides. Mar. Policty 34, 728–732. https://doi.org/10.1016/j.marpol.2009.12.001.

ISA - International Seabed Authority, 2019. Recommendations for the Guidance of Contractors for the Assessment of the Possible Environmental Impacts Arising From Exploration for Marine Minerals in the Area. https://isa.org.jm/files/files/documents/26ltc-6-rev1-en_0.pdf.

Jankowski, J.A., Malcherek, A., Zielke, W., 1996. Numerical modeling of suspended sediment due to deep-sea mining. J. Geophys. Res. Oceans 101 (C2), 3545–3560. https://doi.org/10.1029/95JC03564.

Jones, D.O., Kaiser, S., Sweetman, A.K., Smith, C.R., Menot, L., Vink, A., et al., 2017. Biological responses to disturbance from simulated deep-sea polymetallic nodule mining. PLoS One 12 (2), e0171750. https://doi.org/10.1371/journal.pone.0171750.

Jones, D.O.B., Ardon, J.A., Colaco, A., Durden, J.M., 2020. Environmental considerations for impact and preservation reference zones for deep-sea polymetallic nodule mining. Mar. Policy 118, 103312. https://doi.org/10.1016/j.marpol.2018.10.025.

Kulkarni, C.S., Haley, P.J., Lermusiaux, P.F.J., Dutt, A., Gupta, A., Mirabito, C., et al., 2018. Real-Time Sediment Plume Modeling in the Southern California Bight. OCEANS 2018 MTS/IEEE Charleston, 2018, pp. 1–10. https://doi.org/10.1109/OCEANS.2018.8653642.

Lal, D., 1977. The Oceanic Microcosm of Particles. Sci. New Series 198 (4321), 997–1009. https://doi.org/10.1126/science.198.4321.997.

Lavelle, J.W., Ozturgut, E., Baker, E.T., 1982. Discharge and surface plume measurements during manganese nodule mining tests in the north equatorial pacific. Mar. Environ. Res. 7, 51–70. https://doi.org/10.1016/0141-1136(82)90050-2.

Levin, L.A., Baco, A.R., Bowden, D.A., Colaco, A., Cordes, E.E., Cunha, M.R., et al., 2016. Hydrothermal vents and methane Seeps: rethinking the sphere of influence. Front. Mar. Sci. 3 https://doi.org/10.3389/fmars.2016.00072.

Lohrmann, A., 2001. Monitoring Sediment Concentration with Acoustic Backscattering Instruments, Nortek.

Lucieer, P., Boomsma, W., Broere, B., van Dalfsen, A., de Bruyne, K., Smit, M., de Jonge, L., 2017. Initial design of vehicle propulsion and propulsion test performance. Blue Nodules Public Rep. D2, 4. https://blue-nodules.eu/download/public_reports/public_summary_reports/Blue-Nodules-688975-D2.4-Updated-Initial-design-of-vehicle-propulsion-and-propulsion-test-performanc-FINAL-publishable-summary.pdf.

Masqué, P., Fabres, J., Canals, M., Sanchez-Cabeza, J.A., Sanchez-Vidal, A., Cacho, L., et al., 2003. Accumulation rates of major constituents of hemipelagic sediments in

the deep Alboran Sea: a centennial perspective of sedimentary dynamics. Mar. Geol. 193, 207–233. https://doi.org/10.1016/S0025-3227(02)00593-5.
Mengual, B., Cayocca, F., Le Hir, P., Draye, R., Laffargue, P., Vincent, B., Garlan, T., 2016. Influence of bottom trawling on sediment resuspension in the 'Grande-Vasière' area (Bay of Biscay, France). Ocean Dyn. 66 (9), 1181–1207. https://doi.org/10.1007/s10236-016-0974-7.
Millot, C., 1999. Circulation in the Western Mediterranean Sea. J. Mar. Syst. 20, 423–442. https://doi.org/10.1016/S0924-7963(98)00078-5.
Millot, C., 2009. Another description of the Mediterranean Sea outflow. Prog. Oceanogr. 82 (2), 101–124. https://doi.org/10.1016/j.pocean.2009.04.016.
Mohn, C., Denda, A., Christiansen, S., Kaufmann, M., Peine, F., Springer, B., Turnewitsch, R., Christiansen, B., 2018. Ocean currents and acoustic backscatter data from shipboard ADCP measurements at three North Atlantic seamounts between 2004 and 2015. Data Brief. 17, 237–245. https://doi.org/10.1016/j.dib.2018.01.014.
Perlin, A., Moum, J.N., Klymak, J.M., Levine, M.D., Boyd, T., Kosro, P.M., 2007. Organization of stratification, turbulence, and veering in bottom Ekman layers. J. Geophys. Res. 112 https://doi.org/10.1029/2004JC002641. C05S90.
Peukert, A., Schoening, T., Alevizos, E., Köser, K., Kwasnitschka, T., Greinert, J., 2018. Understanding Mn-nodule distribution and evaluation of related deep-sea mining impacts using AUV-based hydroacoustic and optical data. Biogeosciences 15 (8), 2525–2549. https://doi.org/10.5194/bg-15-2525-2018.
Poulin, P.-M., Menna, M., Gerin, R., 2018. Mapping Mediterranean tidal currents with surface drifters. Deep-Sea Res. I Oceanogr. Res. Pap. 138, 22–33. https://doi.org/10.1016/j.dsr.2018.07.011.
Puig, P., Canals, M., Company, J.B., Martin, J., Amblas, D., Lastras, G., Palanques, A., 2012. Ploughing the deep sea floor. Nature 489 (7415), 286–289. https://doi.org/10.1038/nature11410.
Purkiani, K., Gillard, B., Paul, A., Haeckel, M., Haalboom, S., Greinert, J., et al., 2021. Numerical simulation of Deep-Sea Sediment Transport Induced by a Dredge Experiment in the northeastern Pacific Ocean. Front. Mar. Sci. 8, 719463 https://doi.org/10.3389/fmars.2021.719463.
Renault, L., Oguz, T., Pascual, A., Vizoso, G., Tintore, J., 2012. Surface circulation in the Alborán Sea (western Mediterranean) inferred from remotely sensed data. J. Geophys. Res. 117, C08009. https://doi.org/10.1029/2011JC007659.
Rolinski, S., Segschneider, J., Südermann, J., 2001. Long-term propagation of tailings from deep-sea mining under variable conditions by means of numerical simulations. Deep-Sea Res. II 48, 3469–3485. https://doi.org/10.1016/S0967-0645(01)00053-4.
Sánchez-Garrido, J.C., Sannino, G., Liberti, L., García Lafuente, J., Pratt, L., 2011. Numerical modeling of three-dimensional stratified tidal flow over Camarinal Sill, Strait of Gibraltar. J. Geophys. Res. 116 (C12) https://doi.org/10.1029/2011JC007093.
Simon-Lledo, E., Bett, B.J., Huvenne, V.A.I., Koser, K., Schoening, T., Greinert, J., Jones, D.O.B., 2019. Biological effects 26 years after simulated deep-sea mining. Sci. Rep. 9 (1), 8040. https://doi.org/10.1038/s41598-019-44492-w.
Spearman, J., Taylor, J., Crossouard, N., Cooper, A., Turnbull, M., Manning, A., Lee, M., Murton, B., 2020. Measurement and modelling of deep sea sediment plumes and implications for deep sea mining. Sci. Rep. 10, 5075. https://doi.org/10.1038/s41598-020-61837-y.
Tessier, C., Le Hir, P., Lurton, X., Castaing, P., 2008. Estimation de la matière en suspension à partir de l'intensité rétrodiffusée des courantomètres acoustiques à effet Doppler (ADCP). Compt. Rendus Geosci. 340 (1), 57–67. https://doi.org/10.1016/j.crte.2007.10.009.
Thiel, H., 2001. Evaluation of the environmental consequences of polymetallic nodule mining based on the results of the TUSCH Research Association. Deep-Sea Research II 48, 3433–3452. https://doi.org/10.1016/S0967-0645(01)00051-0.
van Haren, H., 2014. Internal wave–zooplankton interactions in the Alboran Sea (W-Mediterranean). J. Plankton Res. 36 (4), 1124–1134. https://doi.org/10.1093/plankt/fbu031.
Vargas-Yanaz, M., Plaza, F., García-Lafuenta, J., Sarhan, T., Vargas, J.M., Vélez-Belchi, P., 2002. About the seasonal variability of the Alboran Sea circulation. J. Mar. Syst. 35, 229–248. https://doi.org/10.1016/S0924-7963(02)00128-8.
Washburn, T.W., Turner, P.J., Durden, J.M., Jones, D.O.B., Weaver, P., Van Dover, C.L., 2019. Ecological risk assessment for deep-sea mining. Ocean Coast. Manag. 176, 24–39. https://doi.org/10.1016/j.ocecoaman.2019.04.014.
Weaver, P.P.E., Aguzzi, J., Boschen-Rose, R.E., Colaço, A., de Stigter, H.C., Gollner, S., et al., 2022. Assessing plume impacts caused by polymetallic nodule mining vehicles. Mar. Policy 139, 105011. https://doi.org/10.1016/j.marpol.2022.105011.
Yamazaki, T., Kajitani, Y., Barnett, B., Suzuki, T., 1997. Development of image analytical technique for resedimentation induced by nodule mining. In: Second ISOPE Ocean Mining Symposium, Seoul, Korea, November 1997.